# Turbulent Mixing in the Benthic Biolayer of Streams

**Stanley B. Grant[1,2], Jesus D. Gomez-Velez[3], Marco Ghisalberti[4], Ian Guymer[5], Fulvio Boano[6], Kevin Roche[7], Judson Harvey[8]**

[1]Occoquan Watershed Monitoring Laboratory, Department of Civil and Environmental Engineering, Virginia Tech, 9408 Prince William Street, Manassas VA 20110, USA

[2]Department of Civil and Environmental Engineering, University of California Irvine, Irvine, CA 92697, USA

[3]Department of Civil and Environmental Engineering, Vanderbilt University, Nashville, TN 37205, USA

[4]Oceans Graduate School, University of Western Australia, Perth, WA, 6009, Australia.

[5]Department of Civil and Structural Engineering, Sir Frederick Mappin Building, Mappin Street, Sheffield, S1 3JD, England

[6]Department of Environment, Land and Infrastructure Engineering, Politecnico di Torino, Torino 10129, Italy.

[7]Institute of Environmental al Research and Water Research, Spanish National Research Council (CSIC), 08034 Barcelona, Spain

[8]United States Geological Survey, Earth System Processes Division, Reston VA, 20192, USA

Corresponding author: Stanley B. Grant (stanleyg@vt.edu)

**Key Points:**

- Turbulence dominates mixing in the benthic biolayer, the surficial portion of the streambed where pollutants are preferentially removed
- A 1D diffusion model, based on Duhamel's Theorem, is developed and tested for predicting turbulent mass transport in the benthic biolayer
- Mixing in the benthic biolayer increases with the Permeability Reynolds Number, and declines exponentially with depth into the streambed

**Abstract**

Many of the most important ecosystem services performed by streams occur in the benthic biolayer, the biologically active upper ($\leq$10 cm) layer of the streambed. Here we develop and test a rigorous modeling framework, based on Duhamel's Theorem, for the unsteady one-dimensional transport and mixing of a solute in the benthic biolayer of a turbulent stream. The modeling framework is novel in that it allows for depth-varying diffusivity profiles, accounts for the change in porosity across the sediment-water interface and captures the two-way feedback between evolving solute concentrations in both the overlying water column and interstitial fluids of the sediment bed. We apply this new modeling framework to an extensive set of previously published laboratory data, with the goal of evaluating four diffusivity profiles (constant, exponentially declining, and two hybrid models that account for molecular diffusion and enhanced turbulent mixing in the surficial portion of the bed). The exponentially declining and enhanced mixing profiles are superior (based on RMSE, coefficient of determination, and AICc) and their reference diffusivities scale with a dimensionless measure of stream turbulence and streambed permeability called the Permeability Reynolds Number, $\mathrm{Re}_K$. The dependence on $\mathrm{Re}_K$ changes abruptly at $\mathrm{Re}_K = 1$, reflecting different modes of mixing below (dispersion) and above (turbulent diffusion) this threshold value. Because our modeling framework can be applied to open systems (such as streams, lakes, reservoirs, estuaries, and coastal waters), it should inform the prediction and management of pollutant migration through a diverse array of aquatic ecosystems.

## Plain Language Summary

How far and fast pollutants travel downstream is often conditioned on what happens in a thin veneer of bottom sediments called the benthic biolayer. A process level understanding of pollutant mixing and transformation in the benthic biolayer is hampered by the difficulty and expense of measuring representative in-bed solute concentrations. In this paper we develop and test an analytical model from which the evolution of solute concentrations in the benthic biolayer can be inferred from easy to measure solute concentrations in the water column—a key step toward noninvasively characterizing and quantifying pollutant mixing and transformation in the benthic biolayer of streams.

## 1. Introduction

Many physical and biological processes in aquatic ecosystems depend on, or are strongly affected by, turbulent fluid motions at the sediment-water interface (SWI) (Franca and Brocchini, 2015; Grant and Marusic, 2011). Stream turbulence is largely responsible for the drag on streambeds, for example, and thus plays an important role in sediment erosion (Garcia, 2008) and the shear stress environment experienced by benthic flora and fauna (Anim et al., 2019; Kumar et al., 2019; O'Connor et al., 2012; Walsh et al., 2005). Stream turbulence also drives the vertical transport of dissolved constituents through the water column (Tomasek et al., 2018; O'Connor and Hondzo, 2008; Hondzo, 1998), and thereby imposes an upper "speed limit" on the rate that reactive constituents, nitrate for example, can be assimilated and removed by the streambed (Grant et al., 2018a). If the streambed consists of permeable sediments, stream turbulence also facilitates the transport and mixing of dissolved and fine particulate materials and energy across the SWI and into the hyporheic zone, the portion of sediment surrounding a stream where stream water and

groundwater mix (Hester et al., 2017; Krause et al., 2017; Boano et al., 2014; Harvey et al., 2012; Hester and Gooseff, 2010). Steep biochemical and temperature gradients in the hyporheic zone support a unique community of benthic organisms that facilitate key ecosystem functions such as primary production, respiration, nitrification, denitrification, and other transformations of energy-rich constituents (Trauth et al., 2014; Harvey et al., 2013; Zarnetske et al., 2011; Battin et al., 2008; Dahm et al., 2002).

### 1.1 Hyporheic Exchange and the Benthic Biolayer

The movement of stream water into and out of the hyporheic zone, or "hyporheic exchange", occurs over a wide range of spatial (and temporal) scales, from >10 km (>1 year) to <1 m (<1 hr) (Boano et al., 2014; Gomez-Velez and Harvey, 2014; Wörman et al., 2007). This staggering range of scales raises a type of "Goldilocks Dilemma" in which the hyporheic zone's ability to process nutrients from the stream may be compromised if the residence time, reaction time, and exchange rate are too large or small (Harvey et al., 2013). If the residence time is too small, a large fraction of the stream flow may undergo hyporheic exchange (exchange rate large), but the water quality benefit may be limited as nutrients pass through hyporheic zone too quickly to be removed by resident microbial and invertebrate communities. If the residence time is too long, nutrients may be removed as they pass through the hyporheic zone, but the water quality benefits again may not be realized because too small a fraction of the streamflow undergoes hyporheic exchange (exchange rate small). The *just right* condition occurs when the residence time, reaction time, and exchange rate are all in balance (Harvey et al., 2013).

What scale of hyporheic exchange removes the most nutrients? Gomez-Velez et al. (2015) evaluated the residence time/exchange rate trade-off for aerobic respiration and

99 denitrification in the Mississippi River Network, calculating for each reach in the network
100 a so-called Reaction Significance Factor, RSF (Harvey et al., 2013). In the RSF framework,
101 more nutrients are removed when hyporheic zone residence times are similar to reaction
102 times and the uptake length is short compared to the reach length (i.e., the RSF is large).
103 Gomez-Velez et al. found that RSFs were consistently larger for vertical exchange over
104 submerged ripples and dunes (length-scales <1 m) compared to lateral exchange over larger
105 geomorphic features such as river bars and meandering banks (length-scales, >100 m). In
106 other words, the smallest scales of hyporheic exchange appear to be the most important for
107 nutrient processing in streams. This conclusion, which is based on physical arguments (i.e.,
108 a comparison of operative length- and time-scales associated with hyporheic exchange) is
109 reinforced by findings that microbial biomass—as well as nitrification and denitrification
110 potential—tend to be concentrated in the upper ~10 cm of the streambed, a region of the
111 hyporheic zone known as the "benthic biolayer" (Tomasek et al., 2018; Knapp et al., 2017;
112 Caruso et al., 2017). Collectively, these results underscore the importance of elucidating
113 the physical mechanisms responsible for hyporheic exchange at the scale where pollutant
114 transformations predominantly occur; namely, the upper 10 cm of the sediment bed.

115 **1.2 Physical Mechanisms of Turbulent Mixing in the Benthic Biolayer**

116 At the scale of the benthic biolayer, hyporheic exchange is facilitated by at least four
117 mechanisms that are directly linked to, and/or accelerated by, stream turbulence: (1)
118 **"bedform pumping"** arises when dynamic and static pressure variations over the surface
119 of bedforms (e.g., ripples and dunes) drive laminar flow across the SWI in spatially isolated
120 upwelling and downwelling zones (Azizian et al., 2018; Grant et al., 2012; Fleckenstein et
121 al., 2010; Cardenas et al., 2008; Elliot and Brooks, 1997a,b; Thibodeaux and Boyle, 1987);

122 (2) **"turbulent pumping"** occurs when spatially coherent eddies spawn pressure waves
123 that travel along the SWI and drive temporally oscillating laminar flow across the SWI
124 (Roche et al., 2018; Zhong et al., 2016; Boano et al., 2011; Higashino et al., 2009); (3)
125 **"turbulence penetration"** occurs when the penetration of turbulent eddies into the
126 interstitial fluids of the streambed leads to intermittent advective transport across the SWI
127 (Reidenbach et al., 2010; Packman et al., 2004); and (4) **"bedform turnover"** occurs when
128 stress on the streambed, imparted by the turbulent velocity boundary layer, mobilizes
129 unconsolidated sediments, driving the along-channel migration of bedforms and the
130 entrapment and release of interstitial fluids (Zheng et al., 2019; Elliot and Brooks,
131 1997a,b)). Hyporheic exchange is also influenced by heterogeneity in the sediment
132 permeability field (Laube et al., 2018; Salehin et al., 2004; Herzog et al., 2018). While
133 often studied in isolation, it is likely that all four transport mechanisms above contribute,
134 to varying degrees, to the transport and mixing of material and energy across the SWI and
135 in the benthic biolayer of natural streams (**Figure 1a**).

136 **1.3 Conceptual Model of Turbulent Mixing in the Benthic Biolayer**

137 Voermans et al. (2018) proposed a general framework for quantifying the collective
138 contribution of the above transport processes on the horizontally-averaged vertical flux $J$
139 (units of kg per square meter per second) of a conservative (non-reacting) solute through a
140 permeable sediment bed beneath a flowing stream assuming no net advective flux by, for
141 example, groundwater recharge or discharge (Wu et al., 2018; Bhaskar et al., 2012):

142 $$J = -\underbrace{\left(D'_{\mathrm{m}} + D_{\mathrm{d}} + D_{\mathrm{t}}\right)}_{D_{\mathrm{eff}}} \frac{\partial\left(\theta C_{\mathrm{s}}\right)}{\partial x} \qquad (1)$$

143 Variables appearing on the righthand side of this equation represent depth below the SWI
144 ($x$, units of meters), streambed porosity ($\theta$, unitless), and the interstitial concentration of
145 the solute ($C_s$, units of kg per cubic meter) averaged over both the turbulent timescale and
146 the horizontal plane (assumed parallel to the streambed). Here, the flux of mass through
147 the streambed is assumed to be proportional to the vertical concentration gradient and the
148 proportionality constant, or "effective diffusivity" $D_{\text{eff}}$, sums over contributions from the
149 tortuosity-modified molecular diffusion coefficient $D'_{\text{m}}$, the dispersion coefficient $D_{\text{d}}$, and
150 the turbulent diffusion coefficient $D_{\text{t}}$ (all units of square meters per second). The mixing
151 phenomena listed in **Section 1.2**. (bedform pumping, turbulent pumping, turbulence
152 penetration, and bedform turnover) contribute directly to the latter two diffusivities by
153 driving spatial correlations between the time-averaged vertical velocity component and the
154 local mean solute concentration (*dispersion,* $D_{\text{d}}$), and temporal correlations between the
155 turbulent vertical velocity component and the instantaneous turbulent concentration field
156 (*turbulent diffusion,* $D_{\text{t}}$) (Voermans et al., 2018).

157 From refractive index matched particle image velocimetry (RIM-PIV) studies of
158 turbulent motions across the SWI of a permeable streambed (Voermans et al., 2017), these
159 authors also hypothesized that different mixing mechanisms (molecular diffusion,
160 dispersion, turbulent diffusion) dominate the overall effective diffusivity $D_{\text{eff}}$ depending
161 on the magnitude of the Permeability Reynolds number $\text{Re}_K = u_* \sqrt{K} / \upsilon$, a dimensionless
162 representation of the ratio of sediment permeability and viscous length scales that govern
163 turbulence at the SWI. Variables appearing here include a measure of bed shear stress
164 called the shear velocity $u_*$ (units of meters per second), the permeability of the streambed

165 $K$ (units of square meters), and the kinematic viscosity of water $\upsilon$ (units of square meters
166 per second). Mass transport through the sediment bed is dominated by molecular processes
167 at small values of the Permeability Reynolds Number ( $\mathrm{Re}_K < 0.01$ ), dispersion at
168 intermediate values ( $0.01 < \mathrm{Re}_K < 1$ ), and turbulent diffusion at large values ( $\mathrm{Re}_K > 1$ ).
169 Effective diffusivites (estimated from laboratory flume measurements and assuming the
170 diffusivity profile is constant, reviewed by Grant et al. (2012) and O'Connor and Harvey
171 (2008)) are proportional to the square of the permeability Reynolds number ( $D_{\mathrm{eff}} \propto \mathrm{Re}_K^2$ )
172 over a nearly six decade change in the magnitude of $D_{\mathrm{eff}}$ (also see Voermans et al., 2018).

173 **1.4 Experimental Measurements of the Effective Diffusivity**

174 There are several potentially serious problems associated with existing approaches for
175 measuring the effective diffusivity. Laboratory measurements of $D_{\mathrm{eff}}$ involve establishing
176 a disequilibrium between the concentration of a conservative tracer in the sediment and
177 water columns of a closed system (e.g., a stirred tank or recirculating flume, **Figures 1b**
178 and **1c**), and then measuring the rate at which equilibrium conditions are restored. In a
179 typical implementation, the initial state consists of tracer present at a single (well-mixed)
180 concentration in the interstitial fluids of the sediment bed and not in the water column, or
181 vice versa. After an initial start-up period, the evolution of tracer concentration in the water
182 and/or sediment columns is monitored over time for a fixed hydrodynamic condition (e.g.,
183 shear velocity) and streambed composition (e.g., grain size or permeability).

184 Complications arise when these data are reduced to effective diffusivities because,
185 with few exceptions, solutions to the diffusion equation used to reduce these data: 1)
186 assume the effective diffusivity is a fixed constant with depth, and (2) neglect two-way

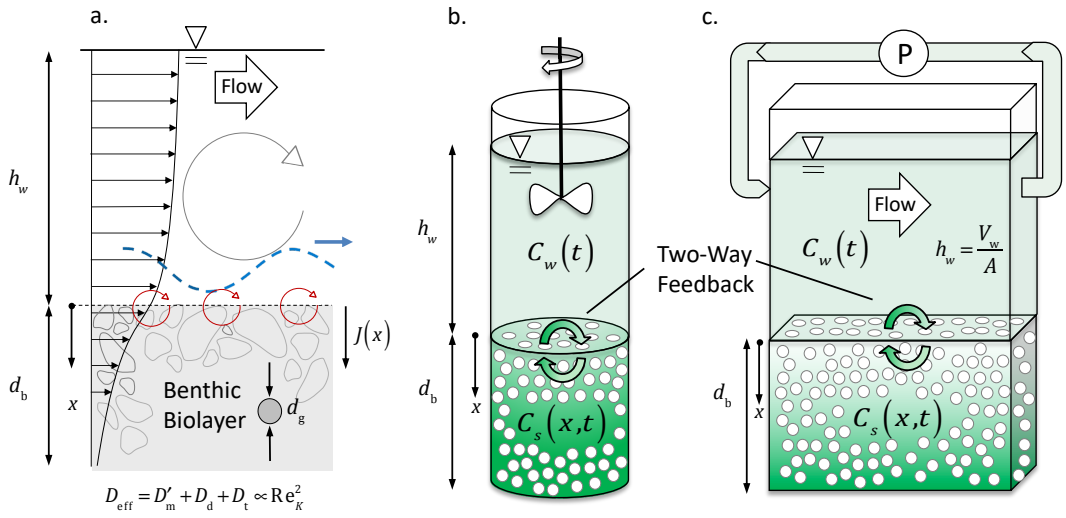


**Figure 1**. (**a**) A conceptual model for the influence of water column turbulence on the mass transport and mixing in the benthic biolayer. In this diagram, the benthic biolayer consists of a flat coarse-grained streambed subject to turbulent pumping (traveling pressure wave, dashed blue line), turbulence penetration (red eddies), and a time-averaged turbulent velocity boundary layer that crosses the sediment-water interface (envelope of black arrows). These turbulence-linked phenomena drive a vertical mass flux $J(x)$ through the benthic biolayer proportional to the concentration gradient at any depth $x$. The proportionality constant, or "effective diffusivity" ($D_{eff}$), is a measure of interstitial transport and mixing by molecular diffusion ($D'_m$), dispersion ($D_d$), and turbulent diffusion ($D_t$). Past studies (which assumed the diffusivity was constant with depth) suggest that the effective diffusivity increases as the square of the Permeability Reynolds Number, $Re_K$. While these processes are of most interest in open systems, such as streams, effective diffusivities are often measured in the laboratory using closed systems, such as stirred tanks (**b**) or recirculating flumes (**c**). The green color in these figures represents the distribution of dye after some elapsed time, assuming it was initially present only in the sediment column. Two-way feedback between evolving concentrations in the water and sediment columns (green arrows in panels (**b**) and (**c**)) decelerates mass transfer across the SWI in both open and closed systems. Variables are defined in the main text.

187

188 feedback between evolving tracer concentrations in the water and sediment columns (green
189 arrows in **Figures (1b)** and **(1c)**).

190 Relative to the first problem, depending on the magnitude of the Permeability
191 Reynolds Number, turbulent mixing across the SWI includes contributions from molecular
192 diffusion, dispersion, and turbulent diffusion (see equation (1) and discussion thereof). It
193 is reasonable to expect that the intensity of the latter two mixing processes will decline
194 with depth, as the influence of water column turbulence, and interactions between the
195 turbulent velocity boundary and roughness features on the streambed, are damped out by
196 viscous dissipation within the porous media—a conclusion supported by in-bed
197 measurements of momentum and mass transfer (Roche et al., 2018; Voermans et al., 2017;
198 Pokrajac and Manes, 2009; Breugem et al., 2006; Nagaoka and Ohgaki, 1990).
199 Incorporating depth-dependent mixing rates into modeling tools (e.g., by letting the
200 effective diffusivity decay with depth) might improve predictions of pollutant transport in
201 streams where turbulence plays an active role in hyporheic exchange (Roche et al., 2019).
202 It might also lead to a better understanding of how turbulent mixing influences, and is
203 influenced by, spatially structured abiotic and biotic streambed processes, such as the
204 zonation of microbial populations responsible for nitrification and denitrification (Kessler
205 et al., 2013; Harvey et al., 2013) and the physical and biological clogging of sediments
206 (Cooper et al., 2018; Newcomer et al., 2016; Stewardson et al., 2016).

207 Relative to the second problem, suppose a conservative solute is initially present in
208 the sediment bed of a closed system with a well-mixed water column (**Figure 1b**). Transfer
209 of mass across the SWI will increase the solute concentration in the water column, reduce
210 the concentration gradient across the SWI (beyond what would be expected if the

increasing water column concentration was not taken into account), and lead to a rapid deceleration of mass transfer across the SWI. Ignoring this two-way feedback, which is an essential feature of mass transfer across the SWI in both open and closed systems (**Section 8**), can bias laboratory estimates of the effective diffusivity. To avoid this problem, experimentalists often adopt ad hoc data analysis procedures, such as restricting the times over which measurements are analyzed (Marion and Zaramella (2005)). Relaxing these assumptions would not only improve experimental estimates of the effective diffusivity, but also permit the exploration of deeper topics, such as the possibility of using measurements in the water column to predict the evolution of hard-to-measure tracer concentrations in the interstitial fluids of the sediment bed.

### 1.5 Approach and Road Map

In this paper we derive and test an analytical modeling framework, based on Duhamel's Theorem, that directly addresses both problems raised above; namely, it allows for a depth-dependent effective diffusivity and encodes the two-way feedback between evolving concentrations above and below the SWI (**Section 2**).

We apply this framework to a set of previously published measurements of mass transfer across the SWI in a well-stirred tank published by Chandler et al. (Chandler et al., 2016; Chandler, 2012) (**Section 3**). Their study is notable for several reasons.

First, it is one of the few where tracer concentrations were simultaneously measured in the water and sediment columns, allowing us to directly compare mixing parameters estimated from data collected exclusively from above or below the SWI.

Second, their 26 experiments cover a large range of bed shear velocities ( $u_* =$ 0.0098 to 0.0407 m $s^{-1}$), mean grain diameters ( $d_g =$ 0.150 to 5.000 mm), sediment

234 permeabilities ($K = 0.18$ to 223 m$^2$), and Permeability Reynolds Numbers, covering both
235 the dispersive and turbulent diffusive mixing ranges ($\mathrm{Re}_K =$ 0.067 to 4.34).

236 Finally, by conceptually dividing the sediment bed into a series of layers and fitting
237 the diffusion equation (with a constant diffusivity profile) to each layer separately,
238 Chandler et al. concluded that the diffusivity declines exponentially with depth. Nagaoka
239 and Ohgaki (1990), who pioneered the approach used by Chander et al., reached a similar
240 conclusion. Furthermore, recent numerical studies by Bottacin-Busolin (2019) suggest that
241 an exponentially declining in-bed diffusivity profile can account for the long-tailed non-
242 Fickian solute breakthrough curves frequently observed in streams.

243 Building on these results, we employed our analytical framework to investigate the
244 relative performance of four diffusivity depth profiles, including: (1) a constant profile
245 (**Section 4**); (2) an exponentially declining profile with or without molecular diffusion as
246 a lower bound (**Section 5**); and (3) an approximation of the "enhanced" diffusivity profile
247 proposed by Roche et al. (2019), in which the diffusivity is constant down to some depth
248 in the sediment bed, below which it declines exponentially (**Section 6**).

249 Our paper concludes with an application of our analytical framework to an open
250 system (**Section 7**) and a summary of conclusions and promising avenues for future
251 research (**Section 8**).

252 **2. Analytical Modeling Framework**

253 In this section we present our theoretical framework for modeling the turbulent mixing of
254 solute across the SWI and through the benthic biolayer, beginning with a description of the
255 one-dimensional diffusion model for transport and mixing in the sediment bed (**Section**
256 **2.1**); a set of solutions, based on Duhamel's Theorem, for mass transfer across the SWI in

257 a closed (**Section 2.2**) or open (**Section 2.3**) system with two-way feedback "turned on"; a
258 corresponding set of solutions with two-way feedback "turned off" (**Section 2.5**); and a set
259 of auxiliary solutions for four different choices of the diffusivity depth profile and two
260 different choices of the lower boundary condition (**Section 2.6**).

261 **2.1 Diffusive Model for Mixing in the Benthic Biolayer**

262 Double averaging over the turbulent timescale and the horizontal plane of the SWI, and
263 assuming that streambed porosity does not change appreciably through the benthic biolayer
264 (i.e., the variable $\theta$ appearing in equation (1) is a fixed constant in the upper ~10 cm of the
265 streambed), the following conservation equation describes the vertical transport and
266 mixing of a conservative (non-reactive) solute in the sediment bed beneath a turbulent
267 stream (Incropera et al., 2007):

268 $$\frac{\partial C_s}{\partial t} = \frac{\partial}{\partial x}\left( D_{\text{eff}}(x) \frac{\partial C_s}{\partial x} \right) \tag{2a}$$

269 New variables appearing here include a depth-varying effective diffusion coefficient
270 ($D_{\text{eff}}(x)$, units of square meters per second) and time ($t$, units of seconds). The coordinate
271 $x$ increases with depth into the streambed, and its origin (at $x = 0$) is positioned at the
272 horizontal plane of the SWI (see **Figure 1a**). Equation (2a) equates the accumulation of
273 mass in any horizontal slice of the streambed ($\theta \partial C_s / \partial t$, left hand side) to the negative
274 divergence of the vertical mass flux $J(x)$ which, in turn, is assumed to follow Fick's First
275 Law:

276 $$J(x) = -\theta D_{\text{eff}}(x) \frac{\partial C_s}{\partial x} \tag{2b}$$

277 In this study we explore several functional forms of the effective diffusivity depth
278 profile, $D_{\mathrm{eff}}(x)=D_{\mathrm{eff},0}f(x)$, where the variable $D_{\mathrm{eff},0}$ is the surficial effective diffusivity (at
279 the SWI, $x=0$) and $f(x)$ (unitless) is a piecewise continuous function that equals unity at
280 the SWI (i.e., $f(0)=1$). After substituting this functional form for the effective diffusivity
281 into equation (2a), the latter can be recast in dimensionless or reduced form, where the new
282 dependent variable $u$ (unitless) incorporates the initial concentration of solute in the
283 interstitial pore fluids of the sediment bed and the overlying water column ($C_{s0}$ and $C_{w0}$,
284 respectively, units of mg per liter):

285 $$\frac{\partial u}{\partial \bar{t}}=\frac{\partial}{\partial \bar{x}}\left(f(\bar{x})\frac{\partial u}{\partial \bar{x}}\right) \qquad (2c)$$

286 $$u(\bar{x},\bar{t})=\frac{C_s(\bar{x},\bar{t})-C_{s0}}{C_{w0}-C_{s0}} \qquad (2d)$$

287 $$\bar{t}=tD_{\mathrm{eff},0}a^2 \ , \quad \bar{x}=xa \qquad (2e)$$

288 The constant $a$ (units of inverse meters) normalizes length-scales in the depth and
289 diffusivity variables. This constant also appears in several of forms of $f(x)$ trialed later,
290 where it is a characteristic length-scale for the decline of diffusivity with depth. Given this
291 definition for $u$ (equation 2d), the initial condition for equation (2c) becomes:

292 $$u(\bar{x},\bar{t}=0)=0 \qquad (3a)$$

293 At the upper boundary (at the SWI, $x=0$) we require that the interstitial tracer
294 concentration equals the stream tracer concentration $C_w$ (units mg per liter), which is
295 assumed to be well-mixed throughout the water column; i.e., $C_w$ depends only on time, not
296 on spatial position in the water column.

297 $$u\left(\overline{x}=0,\overline{t}\right)=\frac{C_w\left(\overline{t}\right)-C_{s0}}{C_{w0}-C_{s0}}\times H\left(\overline{t}\right)=F\left(\overline{t}\right)H\left(\overline{t}\right) \quad (3b)$$

298 $$F\left(\overline{t}\right)=\frac{C_w\left(\overline{t}\right)-C_{s0}}{C_{w0}-C_{s0}} \quad (3c)$$

299 $$H\left(\overline{t}\right)=\begin{cases} 0, & \overline{t}<0 \\ 1, & \overline{t}\geq 0 \end{cases} \quad (3d)$$

300 The dimensionless forcing function $F\left(\overline{t}\right)$ captures the influence of changing water column
301 concentrations on the diffusion equation's upper boundary condition. The Heaviside
302 function $H\left(\overline{t}\right)$ (unitless) is included on the righthand side of equation (3b) to ensure that
303 the forcing function is initially zero (this detail becomes important for the application of
304 Duhamel's Theorem below). By expressing the upper boundary condition in this way, mass
305 transfer across the SWI is assumed to be rate-limited by mixing of solute within the
306 streambed, not by the mixing of solute within the water column; put another way, we are
307 assuming that the Biot Number—which expresses the ratio of diffusive mixing in the
308 streambed to convective mass transfer across the turbulent boundary layer above the
309 streambed—is much less than unity (Incropera et al., 2007).

310 One of two lower boundary conditions can be selected, depending on whether the
311 sediment bed is assumed to be finite (equation (3e)) or infinite (equation (3f)).

312 $$\left.\frac{\partial u}{\partial \overline{x}}\right|_{\overline{x}=\overline{d}_b}=0 \quad (3e)$$

313 $$u\left(\overline{x}\to\infty,\overline{t}\right)=0 \quad (3f)$$

314 Equation (3e) enforces a no-flux boundary condition at reduced depth $\overline{d}_b = a d_b$ (unitless)
315 where $d_b$ (units of meters) is the depth of the sediment bed. Equation (3f) implies that, very
316 deep into the bed ($\overline{x} \to \infty$), the interstitial concentration is maintained at its initial state.

317 **2.2 Water Column Mass Balance in a Closed System**

318 For a closed system with a well-mixed water column (e.g., the configurations shown in
319 **Figures 1b and 1c**), the water column mass balance takes on the following form:

320 $$A h_w \frac{dC_w}{dt} = A\theta D_{\text{eff},0} \left.\frac{\partial C_s}{\partial x}\right|_{x=0,t} \quad (4a)$$

321 New variables appearing here include the sediment bed surface area ($A$, units of square
322 meters) and the height of the water column ($h_w$, units of meters). In the case of a
323 recirculating flume, $h_w$ is an "effective height" equal to the ratio of the total volume of
324 water in the flume's water column and pipes ($V_w$, units of cubed meters) and the bed surface
325 area, $h_w = V_w / A$ (see **Figure 1c**). Failure to account for the porosity of the sediment bed
326 (porosity term on the right hand side of equation (4a)) leads to mass balance errors, and
327 can bias experimental estimates of the effective diffusivity $D_{\text{eff},0}$ downward by up to a
328 factor of ten (Grant et al., 2012). Rewriting equation (4a) using the reduced variables
329 introduced earlier, we obtain the following equation for the forcing function of a closed
330 system with a well-mixed water column:

331 $$\frac{dF}{d\overline{t}} = \frac{1}{\overline{h}_w} \left.\frac{\partial u}{\partial \overline{x}}\right|_{\overline{x}=0,\overline{t}} \quad (4b)$$

332 $$\overline{h}_w = \frac{a h_w}{\theta} \quad (4c)$$

333 The water and sediment column mass balance equations (equations (2a) and (4b),
334 respectively) can be coupled together using Duhamel's Theorem, an analytical approach
335 for solving the diffusion equation in cases where the forcing function at one boundary is a
336 piece-wise continuous function of time (Perez Guerrero et al., 2013). Proofs of this theorem
337 typically assume that the diffusion coefficient is constant (i.e., $f\left(\overline{x}\right)=1$, see equation (1b)).
338 However, as demonstrated in **Appendix A**, the theorem also applies in cases, like those of
339 interest here, where the diffusion coefficient varies solely as a function of depth.

340 For the version of Duhamel's Theorem adopted here, three conditions must be met
341 (Myers, 1971): (1) the system must have a zero initial state; (2) the differential equation
342 and boundary conditions must be homogeneous with the exception of a single time-
343 dependent forcing function in a boundary condition or as a source/sink term of the
344 differential equation; and (3) the single inhomogeneous term should be initially equal to
345 zero. By design, our system meets all three requirements. Namely, the initial condition of
346 the dependent variable is zero ($u\left(\overline{x},\overline{t}=0\right)=0$, see equation (2d)), the differential equation
347 and boundary conditions have only one inhomogeneous term (i.e., the boundary condition
348 at the SWI, equation (3b)), and the inhomogeneous term is initially zero by virtue of the
349 Heaviside function that appears on the right hand side of equation (3b). Accordingly,
350 Duhamel's Theorem allows us to express the evolution of interstitial concentrations in the
351 sediment bed as a convolution integral of the forcing function $F$ and a so-called *auxiliary*
352 *function* $U$ where $v$ is a dummy integration variable (Perez-Guerrero et al., 2013):

353 $$u\left(\overline{x},\overline{t}\right)=\int_0^{\overline{t}}U\left(\overline{x},\overline{t}-v\right)\frac{d}{dv}\left[F\left(v\right)H\left(v\right)\right]dv \qquad (5a)$$

354 The auxiliary function is a solution to the same system of equations described above for
355 mass diffusion through the sediment bed, but with the inhomogeneous term replaced by
356 unity (compare equations (3b) and (5d)):

357 $$\frac{\partial U}{\partial \overline{t}} = \frac{\partial}{\partial \overline{x}}\left( f\left(\overline{x}\right)\frac{\partial U}{\partial \overline{x}} \right) \tag{5b}$$

358 $$U\left(\overline{x}, \overline{t} = 0\right) = 0, \ \overline{x} \geq 0 \tag{5c}$$

359 $$U\left(\overline{x} = 0, \overline{t}\right) = H\left(\overline{t}\right) \tag{5d}$$

360 The lower boundary condition on the auxiliary function will again depend on whether the
361 sediment bed is considered infinite or finite in extent:

362 $$U\left(\overline{x} \to \infty, \overline{t}\right) = 0 \tag{5e}$$

363 $$\left.\frac{\partial U}{\partial \overline{x}}\right|_{\overline{x}=\overline{d}_b} = 0 \tag{5f}$$

364 In typical applications of Duhamel's Theorem, the forcing function $F$ for the
365 inhomogeneous boundary condition is stipulated in advance. In our problem, however, the
366 water column forcing function depends on the interstitial fluid concentration (through the
367 derivative appearing on the right hand side of equation (4b)), while the interstitial fluid
368 concentration depends on the forcing function (through Duhamel's Theorem, equation
369 (5a)); i.e., there is two-way feedback across the SWI. As outlined in **Appendix B**, this
370 feedback can be addressed mathematically by manipulating the water and sediment mass
371 balance equations in the Laplace Domain. The result is a fully coupled set of solutions for
372 solute concentration in the water and sediment columns of a closed stirred tank (equations
373 (T1-1) and (T1-2) in **Table 1**, respectively). In these solutions, the symbol $\mathcal{L}^{-1}\left[\bullet\right]$
374 represents the inverse Laplace Transform, $s$ is the Laplace transform variable, and $\tilde{U}$ is

375 the Laplace transform of the auxiliary function which, in turn, depends on the diffusivity
376 depth profile $f(\bar{x})$ and bottom boundary condition selected. Auxiliary function solutions
377 are presented in **Section 2.5**.

378 [Table 1 goes about here]

379 **2.3 Water Column Mass Balance in an Open System**

380 The application of Duhamel's Theorem described above is restricted to closed stirred tanks;
381 i.e., systems where the water column is well mixed and experiences no exchange of mass
382 with the outside world (e.g., the experimental set-ups illustrated in **Figures 1b** and **1c**). In
383 this section we demonstrate that Duhamel's Theorem can be extended to flow-through
384 stirred tanks, in which solute-free water is added continuously to the water column at a
385 steady volumetric flow rate $Q$ (units of cubic meters per second). To prevent the tank from
386 overflowing, solute-containing water is also withdrawn from the water column at an equal
387 volumetric flow rate. Such flow-through stirred tanks have many analogs in nature,
388 including lakes, lagoons, estuaries, reservoirs, and stream reaches (Oldham et al. (2013);
389 Leibundgut et al. (2009); Vesilind, 1997).

390 The water column mass balance for the flow-through stirred tank configuration is
391 given by equation (6a) (compare with equation (4a)):

392 $$A h_w \frac{dC_w}{dt} = A\theta D_{\text{eff},0} \left.\frac{\partial C_s}{\partial x}\right|_{x=0,t} - Q C_w \qquad (6a)$$

393 Reducing equation (6a) using the same set of dimensionless variables adopted earlier (see
394 equation (4b) and discussion thereof), we arrive at the following equation for the forcing
395 function $F$:

$$\frac{dF}{d\bar{t}} = \frac{1}{\bar{h}_w}\frac{\partial u}{\partial \bar{x}}\bigg|_{\bar{x}=0,\bar{t}} - \frac{1}{\bar{T}}\left[F(\bar{t}) + \frac{C_{s0}}{(C_{w0} - C_{s0})}\right] \tag{6b}$$

$$\bar{T} = D_{\mathrm{eff},0}a^2 T \tag{6c}$$

Here, the "turnover time" $T = h_w A/Q$ is a characteristic timescale for the flushing of solute out of the water column. The reduced turnover timescale, $\bar{T}$, is the ratio of characteristic timescales for the flushing of solute out of the water column and diffusion of solute out of the sediment bed (equation (6c)). It is important to note that the mass balance described here for an open system assumes that the water level $h$ and volumetric flow through the tank $Q$ are both constant; i.e., while the solute concentrations in the water and sediment columns evolve with time, the flow field is assumed to be steady.

Proceeding along the lines described for the closed system in **Appendix B**, we derived a new set of solutions for the evolution of solute concentration in the water and sediment columns of a flow-through stirred tank (equations (T1-5) and (T1-6) in **Table 1**). As the volumetric flow rate through the tank goes to zero (i.e., as the dimensionless turnover time goes to infinity, $\bar{T} \to \infty$), it is easy to show that these new solutions collapse to the closed stirred-tank solutions derived in **Section 2.2** (compare equations (T1-1) and (T1-5), and equations (T1-2) and (T1-6)).

### 2.4 Mass Balance Solutions without Two-Way Feedback.

By invoking Duhamel's Theorem, we captured the two-way feedback characteristic of mass transfer across the SWI in both closed (**Section 2.2**) and open (**Section 2.3**) systems. To isolate the influence of two-way feedback on predicted solute concentrations, it is useful to have a corresponding set of solutions that are identical in all respects, except that the two-way feedback has been "turned off". When two-way feedback is turned off, diffusion

418 of mass across the SWI still affects the mass concentration in the overlying water column,
419 but changes in the water column concentration no longer influence the evolution of
420 interstitial fluid concentrations in the sediment column; i.e., the two-way interaction is
421 reduced to a one-way interaction. Mathematically, two-way feedback can be turned off by
422 changing the upper boundary condition of the diffusion equation such that the interstitial
423 concentration at the SWI is equal, for all time, to some fixed value; for example the initial
424 water column concentration ( $C_s\left(\overline{x}=0,\overline{t}\right)=C_{w0}$ ). Under these conditions, the system of
425 equations for the reduced variable $u$ (equations (3a) through (3f)) is mathematically
426 identical, or isomorphic, to the system of equations for the auxiliary function (equations
427 (5b) through (5f)). Thus, when two-way feedback is turned off, the interstitial solute
428 concentration in the sediment column can be calculated directly from a rearrangement of
429 the auxiliary function (equations (T1-4) and (T1-8) in **Table 1**). A corresponding set of
430 water column solutions (with two-way feedback turned off) are also listed in **Table 1**
431 (equations (T1-3) and (T1-7)).

432 **2.5 Auxiliary Function Solutions**

433 The set of results derived above (and summarized in **Table 1**) are valid for any auxiliary
434 function $\tilde{U}\left(\overline{x},s\right)$ that satisfies equations (5b) through (5f). In **Appendix C** we derive six
435 such auxiliary functions for four different choices of the diffusivity depth profile and two
436 different choices of the bottom boundary condition (infinite or finite sediment bed) (**Table**
437 **2**). The four diffusivity depth profiles considered in this study include (**Figure 2**): (1)
438 constant (*C Profile*, equation (7a)); (2) exponentially declining (*E Profile*, equation (7b));
439 (3) exponentially declining to tortuosity-modified molecular diffusion (*E2M Profile*,
440 equation (7c)); and (4) constant to exponentially declining (*C2E Profile*, equation (7d)).

441 $$f_{\mathrm{C}}\left(\overline{x}\right)=1 \tag{7a}$$

442 $$f_{\mathrm{E}}\left(\overline{x}\right)=e^{-\overline{x}} \tag{7b}$$

443 $$f_{\mathrm{E2M}}\left(\overline{x}\right)=\begin{cases} e^{-\overline{x}},\ 0\le\overline{x}\le\overline{\ell}_m \\ \overline{D}=D'_{\mathrm{m}}/D_{\mathrm{eff},0},\ \overline{x}>\overline{\ell}_m \end{cases},\ \overline{\ell}_m=-\ln\overline{D},\ 0<\overline{D}<1 \tag{7c}$$

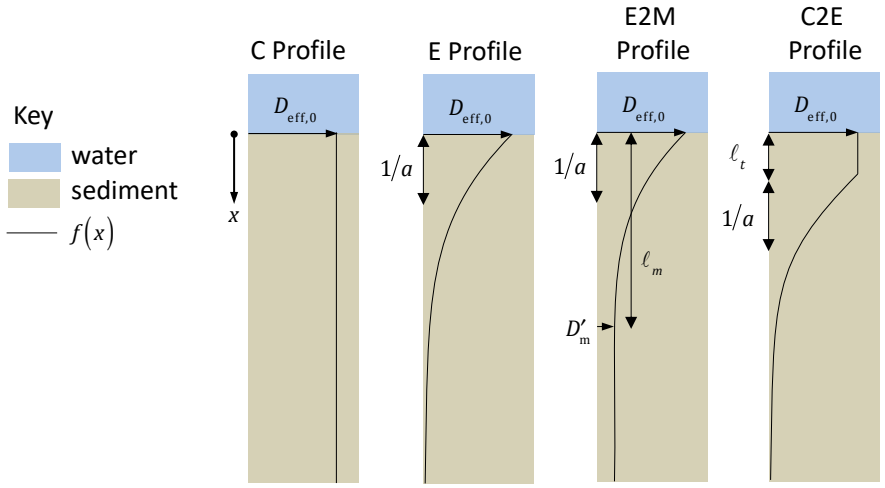


**Figure 2**. Four functional forms of the effective diffusivity profile $f\left(x\right)$ trialed in this study (equations (7a) through (7d)). Variables represent the depth into the sediment bed ($x$), surficial effective diffusivity (at the SWI, $D_{\mathrm{eff},0}$), a decay depth-scale ($1/a$), and the thickness of enhanced mixing at the surface of the sediment bed ($\ell_t$).

444 $$f_{\mathrm{C2E}}\left(\overline{x}\right)=\begin{cases} 1,\ 0\le\overline{x}\le\overline{\ell}_{\mathrm{t}} \\ e^{-\left(\overline{x}-\overline{\ell}_{\mathrm{t}}\right)},\ \overline{x}>\overline{\ell}_{\mathrm{t}} \end{cases} \tag{7d}$$

445 Most laboratory (reviewed in Grant et al. (2012)) and field (Wörman, 2000) studies of
446 diffusive mixing across the SWI adopt the C Profile. However, as noted earlier, several
447 studies (Nagaoka and Ohgaki, 1990; Chandler et al., 2016) have shown that turbulent
448 mixing in the sediment bed declines exponentially with depth, consistent with the E Profile.
449 The E2M profile is a natural extension of the E Profile, accounting for the fact that the
450 tortuosity-modified molecular diffusion coefficient $D'_m$ (units of square meters per second)

451 imposes a lower-bound on the effective diffusivity. E2M's mathematical representation
452 (equation (7c)) includes two new variables: the reduced depth at which the diffusivity
453 profile transitions from exponentially declining to the constant tortuosity-modified
454 molecular diffusion coefficient, $\overline{\ell}_m = a\ell_m$ (unitless) where $\ell_m$ (units of meters) is the
455 transition depth, and a reduced form of the tortuosity-modified molecular diffusion
456 coefficient, $\overline{D} = D'_m / D_{\mathrm{eff},0}$ . These two parameters are mathematically related as follows:
457 $\overline{\ell}_m = -\ln \overline{D}$ . Finally, the C2E Profile captures enhanced mixing at the top of the streambed
458 (similar to Roche et. al, 2019), by extending the surficial effective diffusivity $D_{\mathrm{eff},0}$ to a
459 depth $x = \ell_t$ (units of meters) below the SWI. For depths greater than the enhanced mixing
460 thickness, $x > \ell_t$ , the diffusivity profile declines exponentially. The reduced form of the
461 enhanced mixing thickness $\ell_t$ is defined in the usual way, $\overline{\ell}_t = a\ell_t$ .

462 Together with the seven solutions for $C_w(\overline{t})$ and $C_s(\overline{x},\overline{t})$ presented in **Table 1**
463 (equations (T1-4) and (T1-8) are counted only once, because they are identical), the eight
464 auxiliary function solutions presented in **Table 2** collectively provide 56 different solution
465 combinations for the evolution of solute concentration in the water and sediment columns
466 of a closed or open stirred tank, with or without two-way feedback, and with or without a
467 bottom boundary. In the next several sections we turn to data from a previously published
468 study by Chandler et al. (Chandler, 2012; Chandler et al., 2016) to evaluate the relative
469 performance of the four diffusivity profiles described above and illustrated in **Figure 2**.

470 [Table 2 goes about here]

471 **3. Model-Data Comparisons**

472 **3.1 Measurements of Turbulent Mixing Across the SWI of a Stirred Tank**

473 Similar to the set-up illustrated in **Figure 1b**, Chandler and colleagues studied the turbulent
474 mixing of a conservative tracer (Rhodamine WT) across the SWI of a stirred tank with a
475 flat sediment bed. The stirred tank was an EROSIMESS system (internal diameter of 96.2
476 mm) originally designed to investigate the critical shear stress required to mobilize aquatic
477 sediments (Liem et al., 1997; Sport et al., 1997). Experimental details can be found
478 elsewhere (Chandler, 2012). In brief, the water column depth varied from $h_w =$ 0.25 to 0.26
479 m (depending on the experiment, see **Table S1**), and was turbulently mixed with an
480 impeller attached to the vertical drive shaft of a variable speed motor. The relationship
481 between the rotational velocity of the impeller and the bed shear velocity $u_*$ was estimated
482 by observing the onset of sediment motion and PIV measurements (Chandler, 2012). The
483 sediment column, which had a depth of $d_b = 0.2$ m, consisted of randomly packed single-
484 sized spherical soda glass spheres. In all experiments, the initial state was a Rhodamine
485 saturated sediment bed (concentration of $C_{s0} =$ 100 ppb) and a Rhodamine-free water
486 column ($C_{w0} =$ 0 ppb), although the actual initial concentrations varied somewhat between
487 experiments (**Table S1,** Supplemental Information). Experiments were initiated when the
488 impeller motor was turned on, whereupon tracer concentrations were monitored in the
489 water column and at 5 depths in the sediment column ($x =$ 0.015, 0.049, 0.083, 0.117, and
490 0.151 m below the SWI) at a nominal sampling frequency of 0.1 Hz over a period of hours
491 to days (depending on the experiment). For the purpose of the optimization studies
492 described next, these Rhodamine data were sub-sampled to 30 evenly spaced time points
493 (for the single water column sensor) and 20 evenly spaced time points (for each of the five
494 interstitial fluid sensors), for a total of 130 sub-sampled time points per experiment.

Twenty-three of Chandler et al.'s 26 experiments are included in this study; three experiments were excluded due to missing water column data or other issues.

### 3.2 Parameter Estimation and Model Performance Metrics

Model parameters were estimated for each experiment by minimizing the sum of square error (SSE) calculated from model-predicted and measured Rhodamine concentrations in the water column (equation (8a)) or sediment column (equation (8b)):

$$\mathrm{SSE}_{\mathrm{wat}}\left(\vec{\phi}\right)=\sum_{i=1}^{30}\left[C_w\left(\overline{t}_i;\vec{\phi}\right)-C_{w,\mathrm{meas}}\left(\overline{t}_i\right)\right]^2 \tag{8a}$$

$$\mathrm{SSE}_{\mathrm{sed}}\left(\vec{\phi}\right)=\sum_{j=1}^{5}\sum_{k=1}^{20}\left[C_s\left(\overline{x}_j,\overline{t}_k;\vec{\phi}\right)-C_{s,\mathrm{meas}}\left(\overline{x}_j,\overline{t}_k\right)\right]^2 \tag{8b}$$

New variables appearing here include a vector $\vec{\phi}$ of the base-10 log-transformed diffusivity profile parameters, the number of which varied by diffusivity profile (see **Figure 2**); measured tracer concentrations in the water column at reduced time $\overline{t}_i$ ($C_{w,\mathrm{meas}}\left(\overline{t}_i\right)$, units of mg per liter) and in the sediment column at reduced depth $\overline{x}_i$ and reduced time $\overline{t}_k$ ($C_{s,\mathrm{meas}}\left(\overline{x}_i,\overline{t}_k\right)$, units of mg per liter). The sums are taken over all sub-sampled time points (see Section 3.3) in either the water ($N=30$, equation (8a)) or sediment ($N=20$, equation (8b)) columns, and over the five sensor depths in the sediment column (equation (8b)). For the optimization studies described below, the set of auxiliary function solutions for an infinitely deep sediment bed were adopted (equations (T2-1), (T2-3), (T2-5), and (T2-6) in **Table 2**). We therefore restricted the range of times included in the SSE calculations to those where the measured Rhodamine concentration at the deepest sensor (at $x=0.151$ m) was at least 90% of its initial value. Because the bottom of the bed is at $x=0.2$ m (or 0.049 m below the deepest sensor) this constraint should minimize the influence of the bottom

boundary on the measured and modeled concentration fields. We also excluded the initial time point (at $t = 0$ s) to avoid model singularities. Given these constraints, the 20 or 30 sub-sampled time points (for the sediment sensors or water sensor, respectively) were evenly spaced between elapsed times of $t = 10$ s to $t = t_{final}$, where $t_{final}$ was determined for each experiment according to the 90% criteria above (see **Table S1**).

Log-transformed parameter values were optimized by minimizing equations (8a) and (8b) using the non-linear least squares algorithms implemented within the "NonlinearModelFit" command in the Mathematica computing package (v. 11.20, Wolfram Research, Inc.). This command returns estimates for the mean, standard deviation, and statistical significance of each parameter. Several model performance metrics were also calculated, including the root mean squared error (RMSE), coefficient of determination ($R^2$ value), and the corrected Akaike Information Criterion (AICc). The latter was used to rank the performance of the four diffusivity profiles, accounting for the trade-off between model fit and model complexity. The top-ranked (most parsimonious) model has the smallest AICc value (Aho et al., 2014). The Laplace inversions appearing in **Table 1** were carried using Gaussian Quadrature implemented in the Mathematica package authored by U. Graf (Graf, 2004). As a check on the accuracy of numerical inversions, we verified that numerical estimates of the mass transferred out of the sediment and into the water column agreed within 99.9% or better. All numerical calculations were carried out on UCI's Office of Information Technology High Performance Computing Cluster (https://hpc.oit.uci.edu).

### 3.3 Log-Mean Transforms and Variance Calculations

538 The optimization methods described above yield estimates for the mean and standard
539 deviation of the base-10 log-transformed parameter values, denoted $\mu_{\log_{10}X}$ and $\sigma_{\log_{10}X}$,
540 respectively, where $X$ represents the random variable for the parameter of interest. To
541 avoid introducing statistical bias when converting log-transformed parameter values to
542 arithmetic means (and vice versa), we utilized the standard transformations for a log-
543 normally distributed random variable $X$, where $\ln X = 2.303 \times \log_{10} X$ (Ang and Tang,
544 2007):

545 $$\mu_X = \exp\left[\mu_{\ln X} + \frac{\sigma^2_{\ln X}}{2}\right] \quad (9a)$$

546 $$\sigma_X = \sqrt{\exp\left(2\mu_{\ln X} + \sigma^2_{\ln X}\right)\left(\exp\left(\sigma^2_{\ln X}\right) - 1\right)} \quad (9b)$$

547 $$\mu_{\ln X} = \ln\left[\mu_X \Big/ \sqrt{1 + \sigma^2_X / \mu^2_X}\right] \quad (9c)$$

548 $$\sigma_{\ln X} = \sqrt{\ln\left[1 + \sigma^2_X / \mu^2_X\right]} \quad (9d)$$

549 The first-order approximation of the variance formula was used to propagate parameter
550 error through algebraic and transcendental expressions, assuming uncorrelated variables.
551 When the standard deviation of a constant was not known, a standard deviation was
552 assigned based on an assumed coefficient of variation of 30%.

553 **4. Experimental Evaluation of the C Profile.**

554 In this section we evaluate the performance of the C Profile, which was constructed by
555 substituting equation (T2-1) into equations (T1-1) and (T1-2). Four of the C Profile's six
556 model parameters ($C_{s0}$, $C_{w0}$, $h_w$, $a$, $\theta$, and $D_{eff,0}$) were reported by Chandler et al.,
557 including the initial Rhodamine concentrations in the sediment and water columns

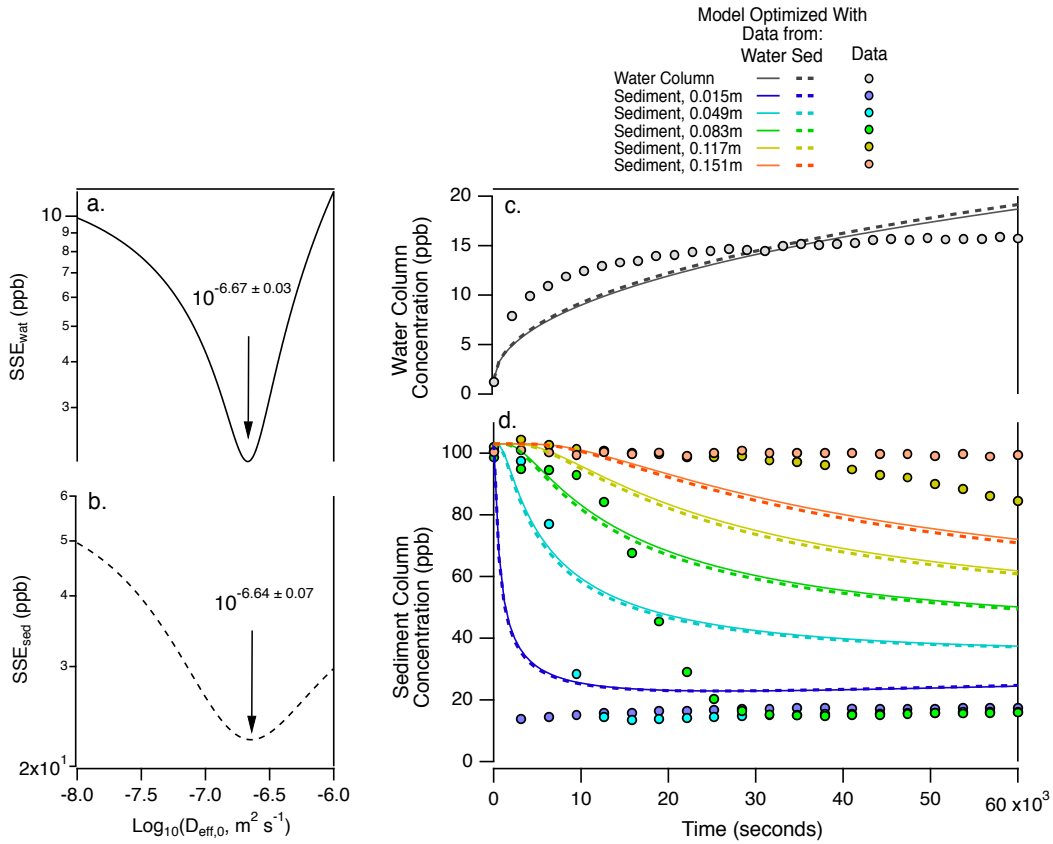


**Figure 3**. A test of the C profile (data from Chandler et al.'s Exp ID 20110405). **(a) and (b)**: Optimal values of the effective diffusivity $D_{\mathrm{eff},0}$ obtained by minimizing the SSE calculated from water (equation (8a), panel (a)) or sediment (equation (8b), panel (b)) column measurements. **(c) and (d)**: Model-predicted (curves) and measured (open circles) tracer concentration in the water column (panel (c)) or sediment column (panel (d)). The curves and data in panel (d) correspond to different depths in the streambed, ranging from near the surface (cool colors) to near the bottom (hot colors) of the bed.

(nominally $C_{s0}$ = 100 ppb and $C_{w0}$ = 0 ppb), water column height ($h_w$ = 0.25 m to 0.26 m) and bed porosity ($\theta$ = 0.38 to 0.39) (see **Table S1** for experiment-specific values). For the C Profile, the inverse length scale $a$ has no physical significance; i.e., whatever value we chose for this parameter cancels off of both sides of the diffusion equation when $f(\bar{x})=1$

562 (see equation (2c)). Thus, for the C Profile, the vector of unknowns $\vec{\phi}$ appearing in
563 equations (8a) and (8b) consists solely of the effective diffusivity, $D_{eff,0}$.

564 **4.1 Experiment ID 20110405**

565 As a first test of the C Profile we focused on a single Chandler et al. experiment
566 (Experiment ID 20110405, $\mathrm{Re}_K = 0.89$) and set out to answer the following question: *is the*
567 *same value of the effective diffusivity* $D_{\mathrm{eff},0}$ *obtained when the C Profile model is optimized*
568 *using only data collected from the water column (by minimizing equation (8a)) versus when*
569 *the model is optimized using only data from the sediment bed (by minimizing equation*
570 *(8b))?* This question is motivated by the desire, articulated earlier, to assess if water column
571 measurements can be used to infer mixing rates in the sediment bed. At least for this
572 particular experiment, the answer appears to be *yes*: effective diffusivities inferred from
573 the water or sediment column measurements agree closely ($D_{\mathrm{eff},0} = 10^{-6.67\pm0.03}$ and $10^{-6.64\pm0.07}$
574 $m^2\ s^{-1}$, respectively) (**Figures 3a**, **3b**).

575 On the other hand, significant bias is evident when model-predicted tracer
576 concentrations (generated with the optimal values of $D_{\mathrm{eff},0}$) are compared with time series
577 measurements of tracer concentration in the water or sediment columns (**Figures 3c** and
578 **3d**). By virtue of the way these experiments were conducted, tracer concentrations in the
579 water column are proportional to the cumulative mass of tracer transferred from the
580 sediment bed to the water column over time. With this in mind, the results plotted in **Figure**
581 **3c** imply that the C Profile model under- and over-estimates mass transfer out of the
582 sediment bed at short and long times, respectively. A comparison of model-predicted and
583 measured tracer concentrations in the sediment bed reveals the underlying problem (**Figure**

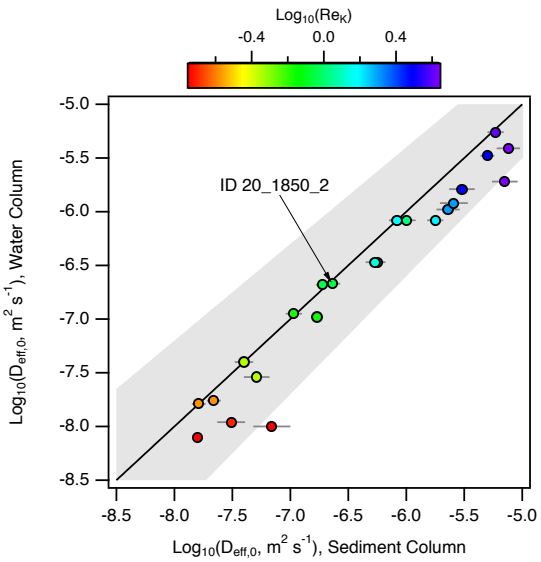


**Figure 4**. Comparison of effective diffusivities estimated by fitting the C profile model only to water column data (vertical axis) or only to sediment column data (horizontal axis). Diagonal line represents a one-to-one relationship; grey band represents +/- 10% of the one-to-one line. Point labeled ID 20110405 corresponds to the experiment analyzed in detail in **Figure 2**. Error bars in the vertical dimension are hidden behind data points.

584 **3d**). The C Profile model under-estimates mixing in the surficial portion of the bed (i.e.,
585 predicted concentrations exceed measured concentrations at $x = 0.015$) and over-estimates
586 mixing deeper in the bed (i.e., predicted concentrations are less than measured
587 concentrations at $x = 0.117$ and 0.151). The former leads to an under-estimation of mass
588 transferred out of the surficial portion of the bed at early times, while the latter leads to an
589 over-estimation of mass transferred out of deeper portions of the bed at later times.

590 **4.2 All 23 of Chandler's Experiments**

591 Across all 23 of Chandler et al.'s experiments, and consistent with the results presented in
592 **Figure 3**, log-transformed diffusivities inferred from Chandler et al.'s water column or
593 sediment column measurements agree within 10% or better (i.e., data points generally fall
594 within the grey band in **Figure 4a**, see **Tables S2** and **S3** in the Supplementary Information

595 for experiment-specific values of $D_{\mathrm{eff},0}$ and the corresponding model performance metrics).
596 However, effective diffusivities inferred from sediment column measurements frequently
597 exceed those inferred from water column measurements, particularly for low and high
598 values of the Permeability Reynolds Number (i.e., 15 of 23 data points in **Figure 4a** plot
599 below the diagonal line).

600 One possible explanation focuses on how Rhodamine concentrations were
601 measured in the interstitial fluids of the sediment bed. As noted earlier (**Section 2**), our
602 analytical framework assumes that the interstitial solute concentrations, $C_s\left(\overline{x},\overline{t}\right)$, are
603 horizontally averaged, while Chandler et al.'s interstitial Rhodamine concentrations are
604 point measurements obtained with fiber optic fluorometers (sensing volumes ca., 0.23 $cm^3$)
605 located on side of the tank (Chandler, 2010). To the extent that these point measurements
606 are not representative of horizontally averaged concentrations (e.g., due to circulation of
607 water and tracer within the streambed) effective diffusivities inferred from our
608 (horizontally averaged) framework are likely to suffer precision and/or accuracy problems.
609 Indeed, Chandler (2010) documented that tracer measurements in the streambed were
610 sensitive to which side of the EROSIMESS system the fluorometers were placed, and these
611 differences appeared consistent over time; i.e., tracer appeared to mix out of the streambed
612 faster on one side of the tank compared to the other side (ibid. pg. 173).

613 Because tracer concentrations measured in the water column reflect mixing rates
614 averaged over the entire surface area of the sediment bed, parameter values inferred from
615 these data are more likely to represent horizontally averaged rates. This idea—that
616 horizontally averaged mixing rates in the sediment column can be inferred solely from
617 measurements in the water column—is intriguing, given the difficulty and expense of

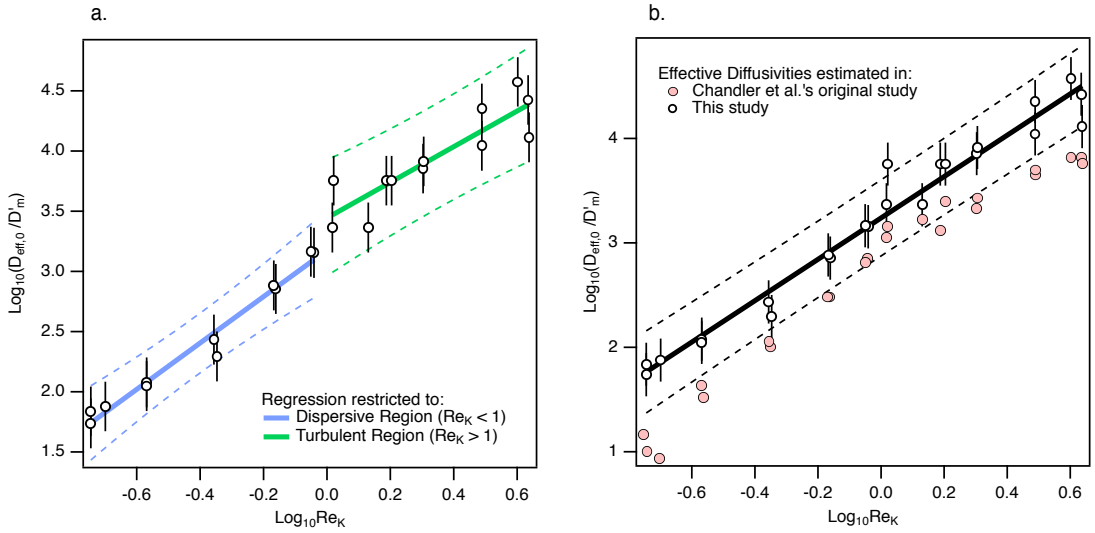


**Figure 5**. **(a)** Permeability Reynolds Number scaling of diffusivities estimated by fitting the C Profile model to Chandler et al.'s water column data. Linear regression results are shown separately for the dispersive (blue line) and turbulent diffusive (green line) regions (equation (10a)). Dashed curves are 95% prediction intervals. **(b)** When the linear regression is carried out on the pooled dataset, effective diffusivities scale as the square of the Permeability Reynolds Number (black open circles and solid line, equation (10b)); dashed curves represent the 95% prediction interval. For comparison, we have also plotted Chandler et al.'s original estimates of the effective diffusivity, obtained by fitting the C Profile model to water column data using the ad hoc procedures described in Section 1 (red filled circles).

obtaining representative measurements of in-bed solute concentrations. It remains to be seen if more physically reasonable forms of the diffusivity depth profile trialed in **Sections 5** and **6** also reduce the model bias evident in **Figure 3**.

### 4.3 Permeability Reynolds Number Scaling of the Effective Diffusivity

As noted earlier, Voermans et al. (2018) hypothesized that the magnitude of the Permeability Reynolds Number indicates whether dispersion ($0.02<\mathrm{Re}_K\leq 1$) or turbulent diffusion ($\mathrm{Re}_K>1$) dominates mixing rates in the sediment bed. To evaluate whether values

of $D_{\mathrm{eff},0}$ inferred from the C Profile scale differently in the dispersion and turbulent diffusion ranges, we separately regressed, over each range, the log-transformed effective diffusivity (normalized by the tortuosity-modified molecular diffusion coefficient for Rhodamine, $D'_m$ ) against log-transformed $\mathrm{Re}_K$ (blue and green lines, **Figure 5a**):

$$\log_{10}\left(\frac{D_{\mathrm{eff},0}}{D'_{\mathrm{m}}}\right)=\begin{cases}(3.18\pm0.26)+(1.93\pm0.54)\times\log_{10}\mathrm{Re}_K,\ R^2=0.974,\ \mathrm{Re}_K<1\\(3.44\pm0.24)+(1.48\pm0.60)\times\log_{10}\mathrm{Re}_K,\ R^2=0.786,\ \mathrm{Re}_K>1\end{cases} \quad (10a)$$

For these calculations, the tortuosity-modified molecular diffusion coefficient ($D'_{\mathrm{m}}=10^{-9.88}$ $\mathrm{m^2\ s^{-1}}$) was estimated by dividing the tortuosity of the sediment bed ($\tau=2.22$) into the molecular diffusion coefficient for Rhodamine in water at 21°C ($D_{\mathrm{m}}=2.9\times10^{-10}$ $\mathrm{m^2\ s^{-1}}$) (Chandler, 2012). The tortuosity of the sediment bed, in turn, was estimated by substituting the measured bed porosity ($\theta=0.39$) into an empirical formula proposed by Iversen and Jorgensen (1992) for sandy beds: $\tau=1+2(1-\theta)$. The intercepts and slopes estimated for the dispersion and turbulent diffusion ranges of the Permeability Reynolds Number have overlapping 95% confidence intervals ($\pm$ values in equation (10a)). Thus, as per Voermans et al. (2018), the effective diffusivities inferred from the C Profile do not appear to scale differently in the dispersion and turbulent diffusion ranges. When the linear regression is repeated with the pooled dataset, the resulting slope ($1.98\pm0.20$) is consistent with a squared dependence on the Permeability Reynolds Number, $D_{\mathrm{eff},0}\propto\mathrm{Re}_K^2$, as previously proposed by Chandler et al. (2016) and Richardson and Parr (1988) (**Figure 5b**):

$$\log_{10}\left(\frac{D_{\mathrm{eff},0}}{D'_{\mathrm{m}}}\right)=(3.24\pm0.09)+(1.98\pm0.20)\times\log_{10}\mathrm{Re}_K,\ R^2=0.967 \quad (10b)$$

644 Our inferred effective diffusivities are about 0.5 log-units larger than Chandler et al.'s
645 published estimates of this parameter (**Figure 5b**), where the latter were obtained following
646 the standard (ad hoc) approach described in **Section 1**.

## 647 5. Experimental Evaluation of the E and E2M Profiles

648 In the last section we found the C Profile model under- and over-estimates mixing in the
649 shallow and deep portions of the bed, respectively, consistent with the hypothesis that the
650 effective diffusivity declines with depth. Here we test this hypothesis by evaluating the
651 experimental performance of the E and E2M Profiles (**Figure 2**). Models for these two
652 profiles were constructed by substituting equation (T2-3) (for the E Profile) and equations
653 (T2-5a), (T2-5b), and (T2-5c) (for the E2M Profile) into equations (T1-1) and (T1-2). In
654 contrast to the C Profile, the parameter $a$ does not cancel off both sides of the diffusion
655 equation (equation (2c)) when $f\left(\overline{x}\right)=e^{-\overline{x}}$. Furthermore, the tortuosity-modified diffusivity
656 appearing in the E2M Profile is known for Chandler et al.'s experiments ($D'_{\mathrm{m}}=10^{-9.88}$ m$^2$ s$^{-1}$
657 [1], see **Section 4.3**). Thus, for both the E and E2M Profiles, the vector $\vec{\phi}$ consists of only
658 two unknowns: the surficial effective diffusivity $D_{\mathrm{eff},0}$ and the inverse depth-scale $a$.

### 659 5.1 The E Profile and Experiment ID 20110405

660 As a first test of the E Profile, we focused on the same dataset analyzed in detail for the C
661 Profile (Chandler et al.'s Experiment ID 20110405, see **Figure 3**), and again asked the
662 question: *are the same parameter values (for the diffusivity profile) obtained when the*
663 *model is optimized with only water or sediment column data?* Here too the answer is *yes*:
664 very similar values for the surficial effective diffusivity ($D_{\mathrm{eff},0}=10^{-5.53\pm0.06}$ or $10^{-5.57\pm0.12}$ m$^2$

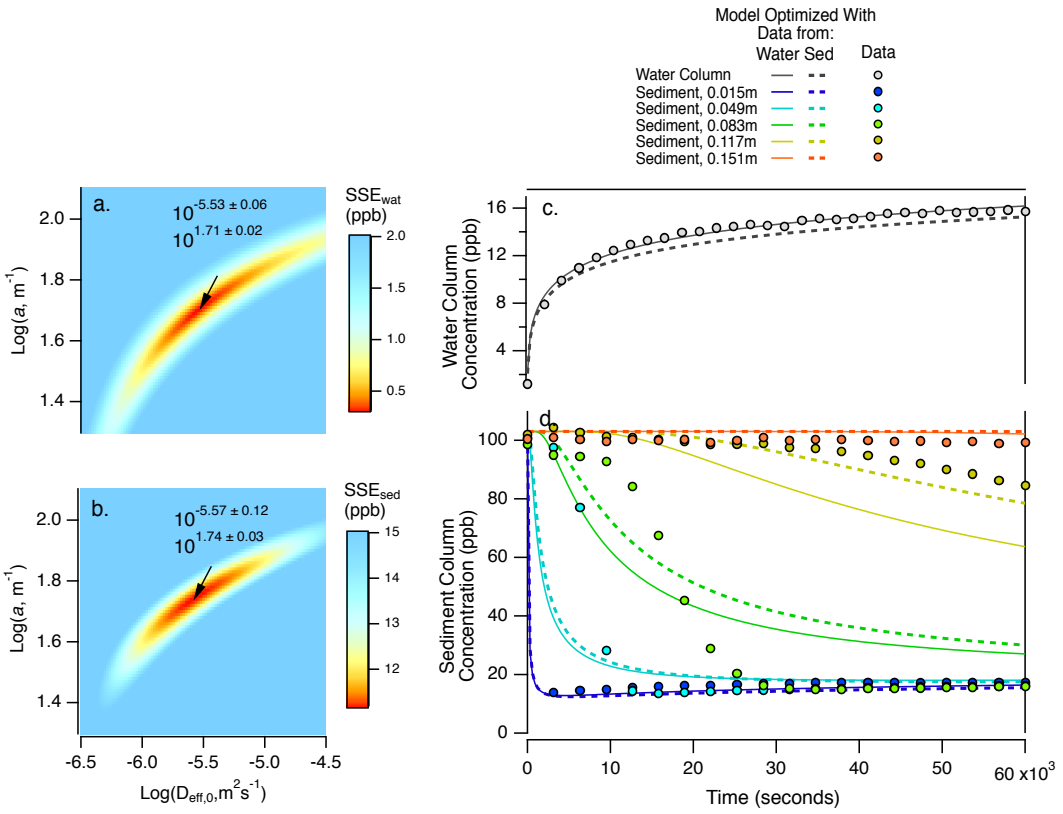


**Figure 6**. A test of the E profile (data from Chandler et al.'s Exp ID 20110405). **Panels (a) and (b)**: Optimal values of the effective diffusivity $D_{\mathrm{eff},0}$ and inverse length-scale $a$ obtained by minimizing the SSE calculated from tracer concentrations measured in the water column (equation (8a), panel (a)) or sediment column (equation (8b), panel (b)). **Panels (c) and (d)**: Model-predicted (curves) and measured (open circles) tracer concentration in the water column (panel (c)) or sediment column (panel (d)).

665 $s^{-1}$) and inverse depth- scale ($a = 10^{1.71 \pm 0.02}$ or $10^{1.74 \pm 0.03}$ $m^{-1}$) are obtained when the E Profile

666 model is optimized using equations (8a) or (8b) (**Figures 6a** or **6b**).

667 Compared to the C Profile and consistent with the hypothesis that the effective

668 diffusivity declines with depth, the E profile shows marked improvement relative to all

669 three performance metrics, including the coefficient of determination (0.9768 versus

670 0.9995), RMSE (2.13 versus 0.31), and AICc (135 versus 22.3) (comparisons based on

671 minimizing $SSE_{wat}$ calculated for the C and E Profiles, respectively, see **Tables S2** and **S4**).

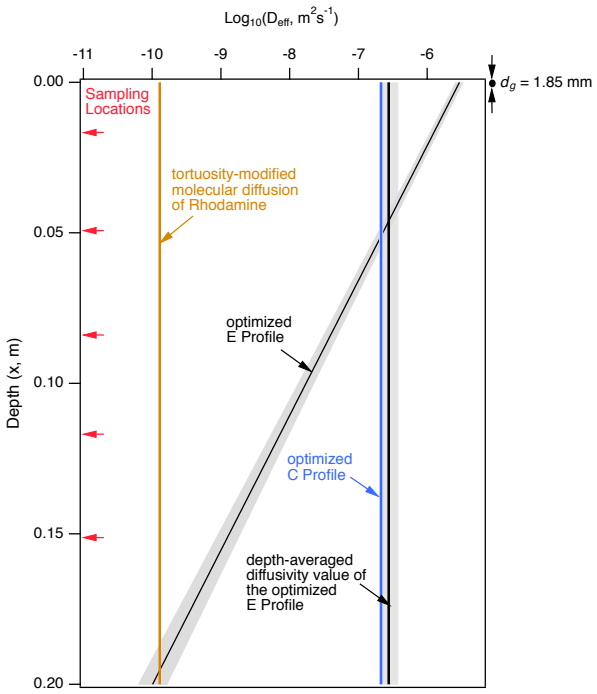


**Figure 7**. The optimized E Profile (black line with grey prediction intervals) and several key mixing constants for Experiment ID 20110405, including the C Profile's optimal diffusivity (light blue vertical line), the depth-averaged diffusivity calculated from the E Profile (vertical black line, equation (11)), and the tortuosity-modified molecular diffusion coefficient of Rhodamine (brown vertical line). Red arrows indicate the depths in the sediment bed where interstitial tracer concentrations were measured by Chandler et al. (2016). Black filled circle indicates the approximate diameter of sediment grains used in this experiment.

The 113 unit drop in AICc is particularly notable, given that a two-unit reduction in this metric is sufficient to declare one model superior to another (Aho et al., 2014). The E Profile model closely tracks the evolution of tracer concentration in the water column (and hence cumulative mass transferred across the SWI, see earlier) (**Figure 6c**), and in the shallow and deep regions of the sediment bed (**Figure 6d**). Some model bias is evident for tracer concentrations at intermediate depths (e.g., at $x = 0.049$ and 0.083 m), likely due to the horizontal variation of interstitial Rhodamine concentration mentioned earlier (see **Section 4.1**).

Substituting optimal values for $D_{\mathrm{eff},0}$ and $a$ (**Figure 6a**) into the E Profile (equation (7b)), the latter predicts a >10,000-fold decline in the effective diffusivity, from approximately $10^{-5.53}$ $m^2$ $s^{-1}$ at the SWI (at $x = 0$ m) to $<10^{-10}$ $m^2$ $s^{-1}$ at $x = 0.2$ m (see line labeled "optimized E Profile"

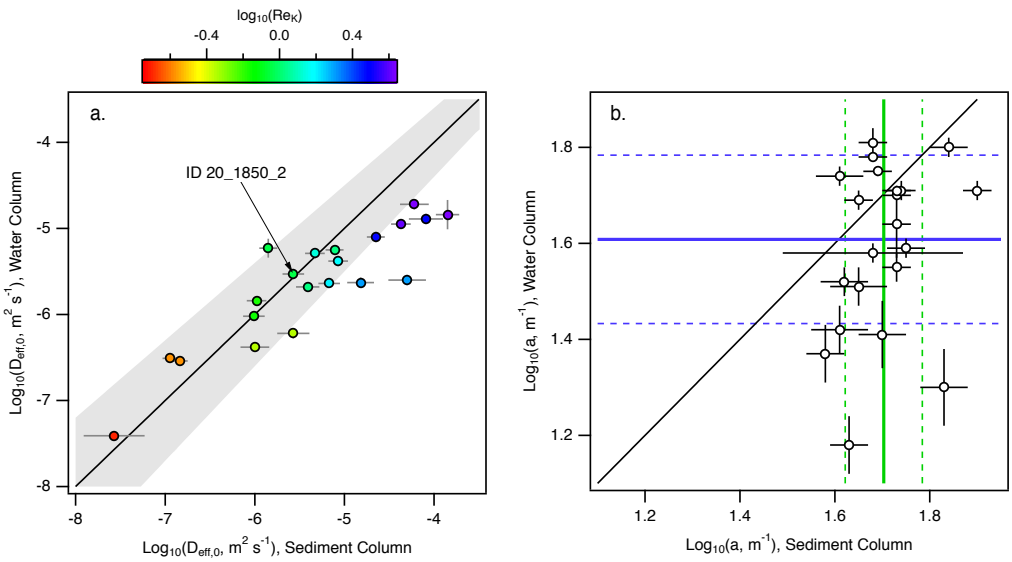


**Figure 8**. **(a)** Comparison of surficial effective diffusivities estimated by fitting the E Profile model only to water (vertical axis) or sediment (horizontal axis) column data. Experiment ID 20110405 was analyzed in detail in **Figures 3** and **6**. Error bars in the vertical dimension are hidden behind data points. **(b)** Comparison of the inverse depth-scales estimated by fitting the E Profile model to water (vertical axis) or sediment (horizontal axis) column measurements. The dark blue and dark green lines represent log-means estimated from the water and sediment column data, respectively (dashed lines are 95% confidence intervals). Diagonal lines in panels (a) and (b) represent a one-to-one relationship; grey band in panel (a) represents +/- 10% of the one-to-one line.

in **Figure 7**). A depth-averaged diffusivity can be calculated from the E Profile by integrating equation (7b), where $d_b = 0.2$ m is the depth of the sediment bed:

$$\overline{D}_{\exp} = \frac{D_{\mathrm{eff},0}}{a\, d_b}\left(1 - e^{-a d_b}\right) \tag{11}$$

Substituting optimized values of $D_{\mathrm{eff},0}$ and $a$ into equation (11), the predicted depth-averaged effective diffusivity ($\overline{D}_{\exp} = 10^{-6.56\pm0.14}$ m$^2$ s$^{-1}$) is equal, within error, to the diffusivity optimized for the same dataset with the C Profile (see **Figure 3a**, $D_{\mathrm{eff},0} = 10^{-6.67\pm0.03}$ m$^2$ s$^{-1}$) (compare blue and black vertical lines, **Figure 7**). Thus, the C and

E Profile models are not only internally self-consistent (i.e., within error, the same profile parameters are inferred when these models are optimized with only water or sediment column data), they are also consistent with each other.

Near the bottom of the sediment bed, below $x \approx 0.195$ m, the exponential diffusivity profile drops below the tortuosity-modified molecular diffusion coefficient for Rhodamine in water, $D'_m = 10^{-9.89}$ m$^2$ s$^{-1}$ (**Figure 7**). Given that this cross-over point occurs within 5 mm of the tank bottom, molecular diffusion is unlikely to have played a significant role in the evolution of Rhodamine concentrations observed in this particular experiment. In principle, however, the effective diffusivity should never fall below the tortuosity-modified diffusion coefficient (see equation (1)); this potential limitation is addressed with the E2M Profile in **Section 5.5**.

### 5.2. All 23 of Chandler's Experiments

Across all 23 of Chandler et al.'s experiments, surficial effective diffusivities $D_{eff,0}$ estimated from the water and sediment columns are correlated (Pearson's correlation coefficient, $R = 0.867$, **Figure 8a**) (see **Tables S4** and **S5** for experiment-specific values of $D_{eff,0}$ and $a$, and corresponding model performance metrics). However, the bias noted previously—where surficial diffusivities estimated from the sediment column data are frequently larger than diffusivities estimated from the water column data, see **Figure 4**—is also evident here, particularly for larger values of the Permeability Reynolds Number (**Figure 8a**). Values of the inverse depth-scale $a$ inferred from the water and sediment column data are not significantly correlated (**Figure 8b**), but their respective log-means ($a = 10^{1.61 \pm 0.18}$ m$^{-1}$ and $a = 10^{1.70 \pm 0.08}$, respectively) are equal within error (see blue and green lines in **Figure 8b**). The corresponding mean and standard deviation of the inverse depth-

725 scale (obtained by applying equations (9a) and (9b) to the log-mean results) are
726 $a = 44.0 \pm 18.5$ m$^{-1}$ and $a = 51.4 \pm 9.71$ m$^{-1}$, respectively. These values are similar to the
727 inverse depth-scale reported by Chandler et al. (2016) of $a = 55$ m$^{-1}$.

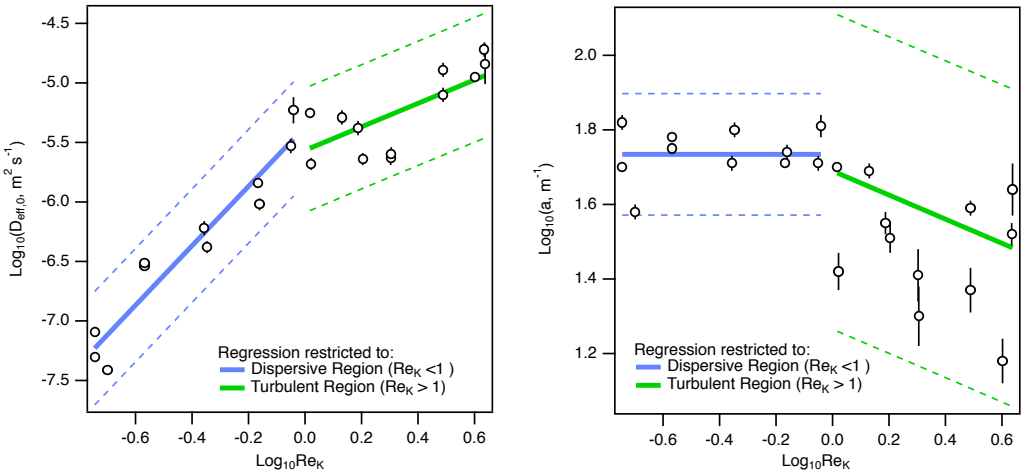


**Figure 9**. Permeability Reynolds Number scaling of the E Profile's two parameters, estimated from Chandler et al.'s water column measurements. The surficial diffusivity **(a)** and inverse decay length-scale (**b**) follow different scaling relationships in the dispersive (blue lines) and turbulent diffusive (green lines) ranges. Dashed curves are 95% prediction intervals.

728 **5.3 Permeability Reynolds Number Scaling Behavior**

729 In Section 4.2 we found that $D_{\mathrm{eff},0}$ values inferred from the C Profile model are proportional
730 to the square of the Permeability Reynolds Number across the latter's full range (see
731 **Figure 5b**). By contrast, when surficial effective diffusivities inferred from the E Profile
732 are plotted against the Permeability Reynolds Number, a significant change in slope and
733 intercept (as represented by non-overlapping 95% confidence intervals in equation (12a))
734 is evident around $\mathrm{Re}_K = 1$ (**Figure 9a**).

$$\log_{10}\left(D_{\text{eff},0},\ \text{m}^2\text{s}^{-1}\right)=\begin{cases}\left(-5.37\pm0.07\right)+\left(2.50\pm0.11\right)\times\log_{10}\text{Re}_K,\ R^2=0.949,\ \text{Re}_K<1\\ \left(-5.57\pm0.06\right)+\left(0.99\pm0.15\right)\times\log_{10}\text{Re}_K,\ R^2=0.440,\ \text{Re}_K>1\end{cases} \tag{12a}$$

The power-law exponent for the surficial effective diffusivity declines from $2.50\pm0.11$ in the dispersive mixing range ($\text{Re}_K<1$) to $0.99\pm0.15$ in the turbulent mixing range ($\text{Re}_K>1$). Likewise, the scaling behavior of the inverse depth-scale transitions from a constant value ($a=10^{1.73\pm0.01}\ \text{m}^{-1}$) in the dispersive range to a weak inverse dependence on the Permeability Reynolds Number ($a\propto\text{Re}_K^{-0.32\pm0.08}$) in the turbulent range (**Figure 9b**):

$$\log_{10}\left(a,\ \text{m}^{-1}\right)=\begin{cases}1.73\pm0.01,\ \text{Re}_K<1\\ \left(1.69\pm0.02\right)-\left(0.32\pm0.08\right)\times\log_{10}\text{Re}_K,\ R^2=0.18,\ \text{Re}_K>1\end{cases} \tag{12b}$$

To put these latter results in context, the corresponding "$1/e$-folding depths" (i.e., the depth at which the E Profile's effective diffusivity declines to $1/e\approx0.37$ of its surficial value) range from $x=0.015$ m ($a=10^{1.82}$ m$^{-1}$) to $x=0.066$ m ($a=10^{1.18}$ m$^{-1}$) with increasing Permeability Reynolds Number. These $1/e$-folding depths are all less than the depth of the sediment bed ($d_b=0.2$ m) suggesting that the former is not pre-determined by the latter.

The scaling relationship for the surficial effective diffusivity (equation (12a)) can also be written in reduced form, permitting a direct comparison with the C Profile scaling law developed in **Section 4.3** (compare with equation (10b)):

$$\log_{10}\left(D_{\text{eff},0}/D'_m\right)=\begin{cases}\left(4.50\pm0.18\right)+\left(2.42\pm0.36\right)\times\log_{10}\text{Re}_K,\ R^2=0.889,\ \text{Re}_K<1\\ \left(4.27\pm0.16\right)+\left(1.13\pm0.42\right)\times\log_{10}\text{Re}_K,\ R^2=0.564,\ \text{Re}_K>1\end{cases} \tag{12c}$$

When comparing equations (10b) and (12c), it is important to recall the different definitions of the surficial diffusivities $D_{\text{eff},0}$ employed for these two profiles; i.e., for the C Profile

753 (equation (10)) it is a fixed constant throughout the sediment column, while for the E
754 Profile (equation (12c)) it is the value of the effective diffusivity at the SWI. Because the
755 E Profile's effective diffusivity decays with depth, all else being equal, $D_{\mathrm{eff},0}$ values
756 inferred from the E Profile should be larger than $D_{\mathrm{eff},0}$ values inferred from the C Profile,
757 consistent with observations (**Figure 10**).

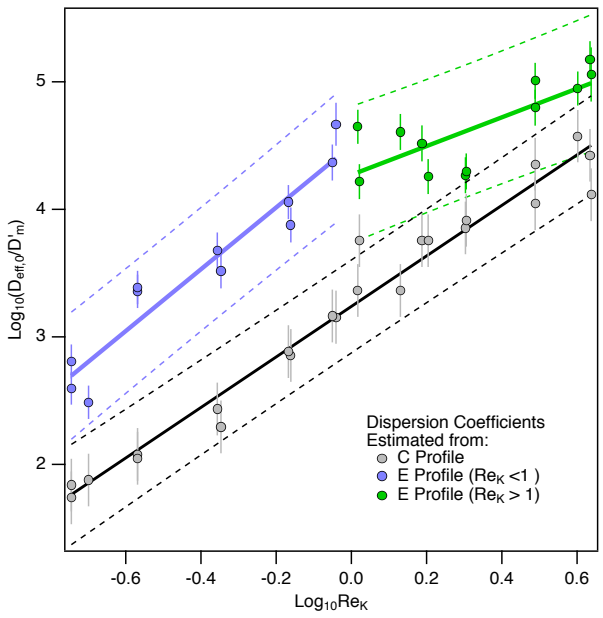


**Figure 10**. A comparison of the surficial effective diffusivities inferred from the C Profile (grey points) and E Profile (blue and green points). The former has a single scaling relationship (black line, equation (10b)), while the latter has separate scaling relationships in the dispersive (blue line) and turbulent (green line) ranges (equation (12c)). Dashed curves are 95% prediction intervals.

How much larger depends on the value of the inverse depth-scale $a$. This can be demonstrated by examining the E Profile's estimate for the depth-averaged effective diffusivity $\overline{D}_{\mathrm{exp}}$ (equation (11)), which we have already noted can be taken as an approximation of the C Profile's $D_{\mathrm{eff},0}$ (compare blue and black vertical lines in **Figure 7**). According to equation (11), the surficial and depth-averaged effective diffusivities converge ($\overline{D}_{\mathrm{exp}} \to D_{\mathrm{eff},0}$) as the inverse depth-scale becomes small (this can be confirmed by expanding equation (11) in powers of $a$, and taking the limit $a \to 0$). Conversely, when the inverse depth-scale is large ($a \to \infty$)

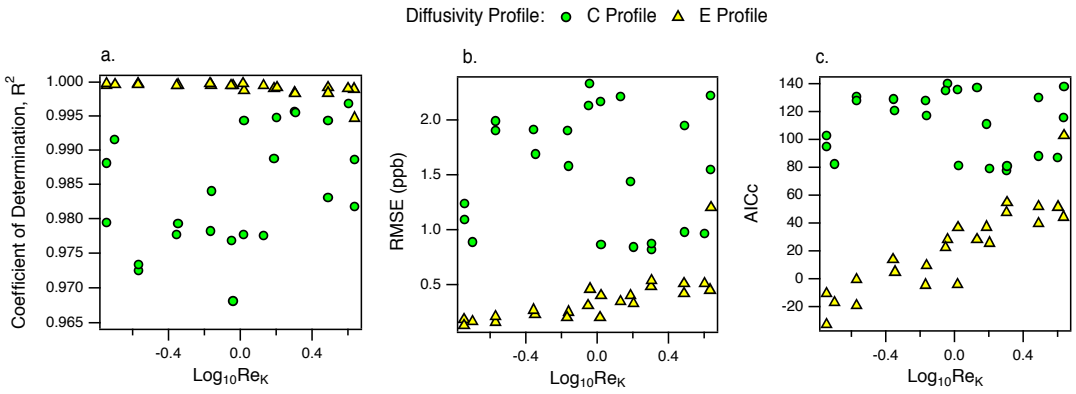


**Figure 11**. The relative performance of C and E Profile models across all 23 of Chandler et al.'s stirred tank experiments. Model performance metrics include the (**a**) coefficient of determination, $R^2$, (**b**) Root Mean Square Error, RMSE, and (**c**) Akaike's Information Criterion, AICc.

equation (11) predicts that the surficial effective diffusivity exceeds the depth-averaged effective diffusivity by a factor of about $ad_b$. Both predictions are consistent with the results presented in **Figure 10**. In the dispersion range ($\mathrm{Re}_K < 1$) the inverse length scale $a$ is relatively large and constant (see **Figure 9b**) and the values of $D_{\mathrm{eff},0}$ inferred from the E Profile are about $ad_b \approx 11$ times larger than values inferred from the C Profile (compare blue and grey points, **Figure 10**). In the turbulent range ($\mathrm{Re}_K > 1$) the inverse depth-scale $a$ declines with increasing $\mathrm{Re}_K$ (**Figure 8b**), and the C and E Profile's inferred values of $D_{\mathrm{eff},0}$ converge with increasing $\mathrm{Re}_K$ (compare green and grey points, **Figure 10**).

### 5.4. Relative Performance of the C and E Profiles.

Based on a detailed analysis of Chandler et al.'s Exp ID 20110405 in **Section 5.1**, we concluded that the E Profile represents a substantial improvement over the C Profile. This conclusion extends to the rest of Chandler et al.'s experiments as well (**Figure 11** and **Tables S2** – **S5**). In all cases, the E Profile model captures a larger fraction of data variance

788 (generally in excess of 99.9%) and has substantially smaller RMSE and AICc values
789 (**Figures 11a** and **11b**). Despite its increased complexity (the C and E Profiles have one
790 and two unknown parameters, respectively) the AICc is also consistently 80 to 140 units
791 lower for the E Profile model (**Figure 11c**), implying that it is the superior model.

792 **5.5 Experimental Evaluation of the E2M Profile.**

793 While the E Profile is a dramatic improvement over the C Profile, it is interesting to note
794 that its coefficient of determination decreases, and both RMSE and AICC increase, as the
795 Permeability Reynolds Number increases (**Figure 11**). This raises the question: *can the E*
796 *Profile's performance be improved by explicitly accounting for the lower bound on the*
797 *effective diffusivity imposed by molecular diffusion; i.e., by replacing the E Profile with the*
798 *E2M Profile?* The answer is *no*: across all 23 of Chandler et al.'s experiments, inferred
799 values of $D_{\mathrm{eff},0}$ and $a$ (**Figure S1, Supplemental Information**) and performance metrics
800 (compare coefficient of determination, RMSE, and AICc, **Tables S4** and **S6**) for the E and
801 E2M Profile models are nearly identical.

802 To understand why including molecular diffusion did not change our optimization
803 results, for each of Chandler et al.'s experiments we estimated the depth at which the
804 diffusivity profile transitions to the tortuosity-modified molecular diffusion coefficient,
805 $\ell_m = -\ln\bar{D}/a$ where $\bar{D} = D'_{\mathrm{m}}/D_{\mathrm{eff},0}$ (see equation (7c) in **Section 2.5**). These molecular
806 diffusion transition depths, which range from 6 to 56 cm ($\ell_m = 10^{-1.2}$ to $10^{-0.25}$ m), increase
807 roughly with the square root of the Permeability Reynolds Number ($\ell_m \propto \sqrt{\mathrm{Re}_K}$, **Figure**
808 **12a**):

809 $$\log_{10}(\ell_m,\ \mathrm{m}) = (-0.78 \pm 0.15) + (0.49 \pm 0.36) \times \log_{10}\mathrm{Re}_K,\ R^2 = 0.809 \qquad (13)$$

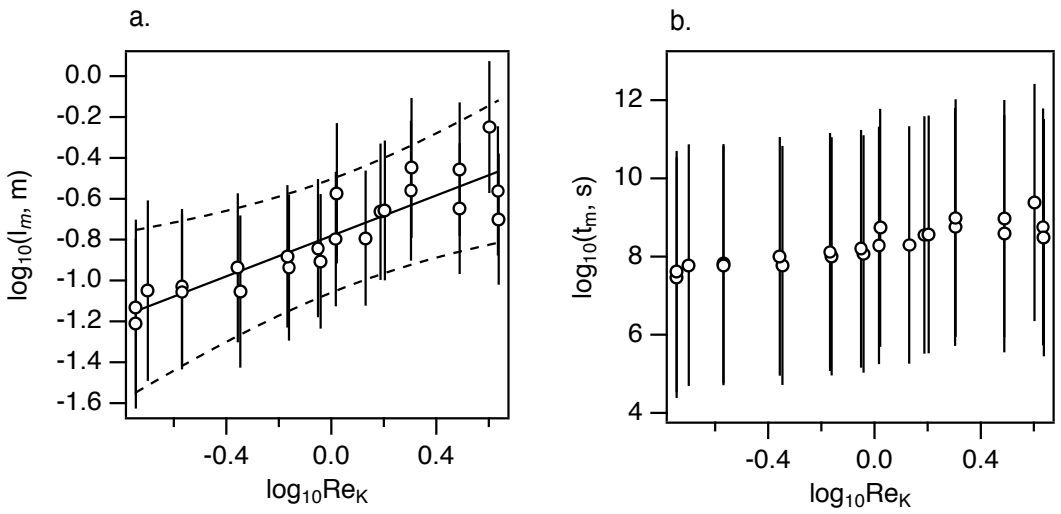


**Figure 12**. (**a**) E2M Profile predictions for the depth at which molecular diffusion begins to dominate the vertical transport and mixing of tracer, plotted against the Permeability Reynolds Number (regression line corresponds to equation (13), dashed curves are the 95% prediction interval). (**b**) Corresponding timescales for mass transport through the interstitial fluids of the sediment bed by molecular diffusion.

*810* The corresponding times required for mass transport to occur across these distances by
*811* molecular diffusion alone ($t_m = \ell_m^2 / D'_m$) are all greater than 11 months ($>10^{7.5}$ s) (black
*812* circles, **Figure 12b**)). Thus, for the range of Permeability Reynolds Numbers investigated
*813* by Chandler et al., experiments would have had to continue for more than one year to
*814* observe the effect of molecular diffusion on mass transport across the SWI. While the E2M
*815* Profile is not an improvement in this specific set of experiments, it could be useful in
*816* settings (low permeability sediments and/or low shear velocity) where the Permeability
*817* Reynolds number is very small in magnitude.

*818* **6. Experimental Evaluation of the C2E Profile.**

*819* In this section we test the hypothesis that the performance of the E Profile can be improved
*820* by allowing for "enhanced mixing" in the surficial portion of the sediment bed, represented

821 here by the C2E Profile (**Figure 2**). The C2E Profile model was constructed by substituting
822 equations (T2-6a) and (T2-6b) into equation (T1-1). Its parameter vector $\vec{\phi}$ has three
823 unknowns: the surficial effective diffusivity $D_{\mathrm{eff},0}$, the inverse depth-scale $a$, and the
824 enhanced mixing thickness, $\ell_t$ (**Figure 2**).

825 **6.1 C2E Profile and Experiment ID 20110405**

826 As a first test of the C2E Profile model, we focused on the single experiment (Experiment
827 ID 20110405, $\mathrm{Re}_K = 0.89$) discussed in **Sections 4** and **5**. Minimization of the water column
828 SSE yield clearly defined optima for the log-transformed values of the surficial effective
829 diffusivity ( $D_{\mathrm{eff},0} = 10^{-6.13\pm0.02}$ m$^2$ s$^{-1}$), inverse depth-scale ( $a = 10^{1.92\pm0.03}$ m$^{-1}$) and the
830 enhanced mixing thickness ( $\ell_t = 10^{-1.33\pm0.03}$ m) (**Figures 13a, b,** and **c**, respectively). As
831 might be expected given that the C2E Profile is a hybrid of the C and E Profiles, the
832 effective diffusivity ( $D_{\mathrm{eff},0} = 10^{-6.13\pm0.02}$ m$^2$ s$^{-1}$) inferred from the C2E Profile is intermediate
833 between effective diffusivities inferred from the C Profile ( $D_{\mathrm{eff},0} = 10^{-6.67\pm0.03}$ m$^2$ s$^{-1}$, **Section**
834 **4.1**) and from the E Profile ( $D_{\mathrm{eff},0} = 10^{-5.53\pm0.06}$ m$^2$ s$^{-1}$, **Section 5.1**).

835 To compensate for increased mixing in the surficial region of the sediment bed
836 (over $0 \le x \le \ell_t$), the C2E Profile's inverse depth-scale ( $a = 10^{1.92\pm0.03}$ m$^{-1}$) and $1/e$-folding
837 depth ( $1/a = 1.2\pm0.08$ cm) are significantly larger and smaller, respectively, compared to
838 corresponding values inferred from the E Profile ( $a = 10^{1.71\pm0.02}$ m$^{-1}$ and $1/a = 1.9\pm0.09$ cm,
839 see **Section 5.2**).

840 The enhanced mixing thickness $\ell_t = 4.7\pm0.3$ cm (obtained by applying equations
841 (9a) and (9b) to the log-transformed optimal value shown in **Figure 13c**) is about 25 times

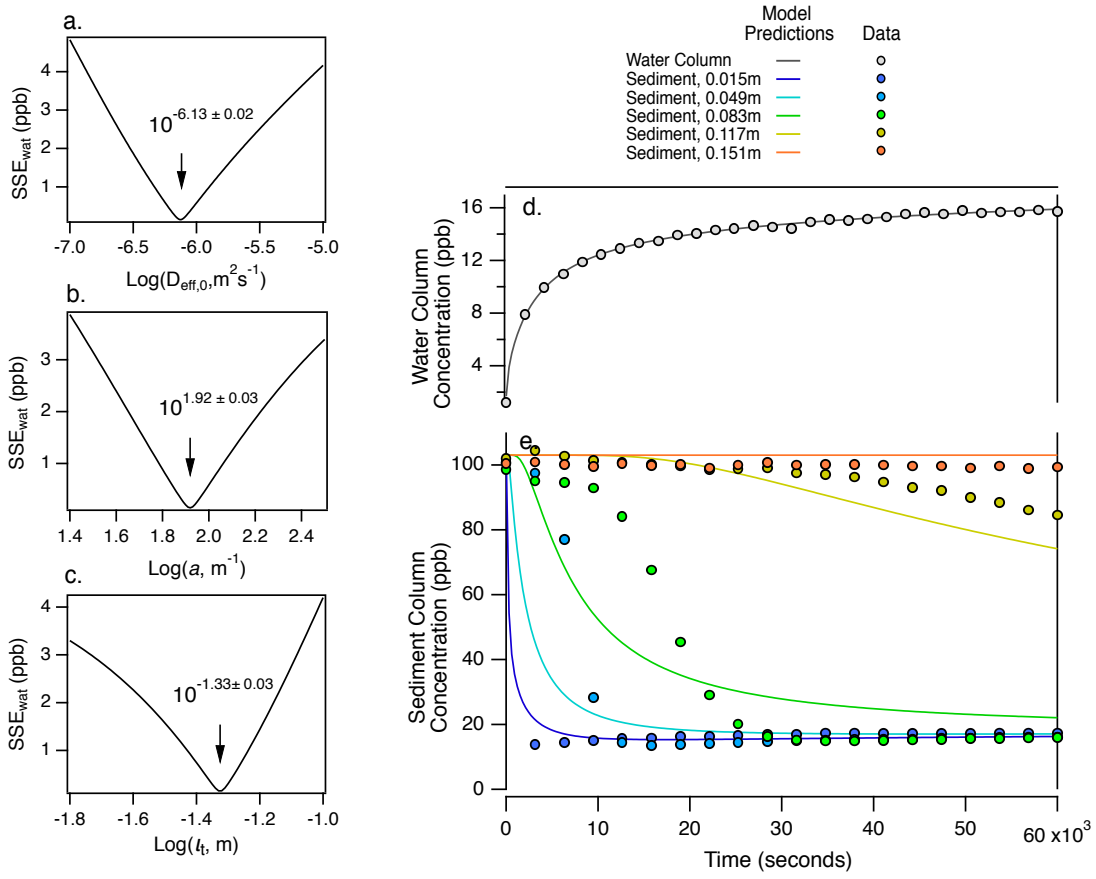


**Figure 13**. A test of the C2E Profile model (data from Chandler et al.'s Exp ID 20110405). Optimal values of the (**a**) effective diffusivity $D_{\mathrm{eff},0}$, (**b**) inverse depth-scale $a$, and (**c**) the enhanced mixing thickness $\ell_t$ obtained by minimizing $\mathrm{SSE}_{\mathrm{wat}}$ (equation (8a)). Model-predicted (curves) and measured (open circles) tracer concentration in the water (**d**) or sediment (**e**) columns.

larger than the diameter of the glass spheres that make up the sediment bed ($d_g = 1.85$ mm) and about 50 times larger than the Brinkman Layer thickness, $\delta_b \approx 20\sqrt{K} = 0.9$ mm, where the latter is an estimate for the depth to which the time-averaged turbulent velocity boundary layer penetrates into the streambed (Voerman et al.'s 2017). These comparisons raise the question: *what is the physical interpretation of the enhanced mixing thickness* $\ell_t$*?*

847 Based on a model for mass exchange across the SWI by turbulent pumping (see
848 **Section 1**) Higashino et al. (2009) reported that, at depths similar to $\ell_t \approx 5$ cm and for shear
849 velocities between $u_* = 0.01$ and $0.02$ m s$^{-1}$, the root mean square (RMS) vertical pore
850 velocities are between 1 and 10% of their value at the SWI (ibid, Figure 3). Thus, one
851 plausible interpretation is that $\ell_t$ represents the depth into the surficial portion of the
852 streambed over which tracer mass is vigorously mixed by turbulent pumping. We will
853 return to this idea in **Section 6.3**.

854 The C2E profile outperforms the E Profile relative to all three model performance
855 metrics, including the coefficient of determination (0.9995, 0.9999), RMSE (0.31, 0.145),
856 and AICc (22.3, -21.1) (comparisons based on minimizing $SSE_{wat}$ for the E and C2E
857 Profiles, respectively). The 43 unit drop in AICc indicates the C2E Profile is a substantial
858 improvement over the E Profile, even after accounting for the former's increased
859 complexity (three versus two unknown parameters). Tracer concentrations predicted with
860 the C2E Profile model are in near perfect agreement with tracer concentrations measured
861 in the water column (and hence cumulative mass transferred across the SWI, see earlier)
862 (**Figure 13d**), and closely track measured interstitial tracer concentrations in the shallow
863 and deep regions of the sediment bed (**Figure 13e**). Model bias is evident for tracer
864 concentrations at intermediate depths (e.g., at $x =$ 0.049 and 0.083 m, similar to the
865 behavior noted earlier for the E Profile), perhaps due to horizontal variations in the
866 interstitial Rhodamine concentration (see discussion in **Section 4.2**).

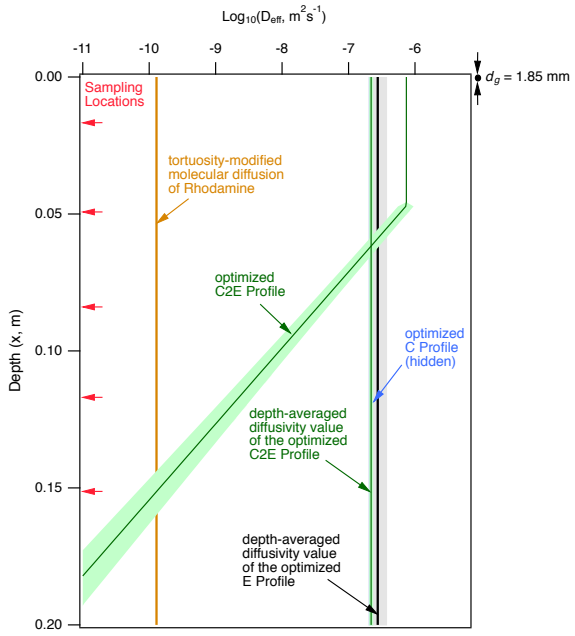


**Figure 14**. The optimized C2E Profile (green line and prediction intervals) compared to several key mixing constants, including the optimal diffusivity inferred from the C Profile (light blue vertical line), the depth-averaged diffusivity inferred from the E Profile (vertical black line, equation (11)), the depth-averaged diffusivity inferred from the C2E Profile (vertical green line, equation (14)) and the tortuosity-modified molecular diffusion coefficient of Rhodamine (brown vertical line). Red arrows indicate the depths in the sediment bed where interstitial tracer concentration was measured by Chandler et al. Black circle indicates the approximate diameter of quartz spheres used for the sediment bed in this experiment.

Substituting the optimal values for $D_{\mathrm{eff},0}$, $a$, and $\ell_t$ into equation (7d), the C2E Profile predicts a greater than five decade decline in the effective diffusivity, from $10^{-6.13}$ m$^2$ s$^{-1}$ at the SWI (at $x = 0$ m) to less than $10^{-11}$ m$^2$ s$^{-1}$ at base of the sediment bed ($x = 0.2$ m, see green line labeled "optimized C2E Profile" in **Figure 14**). A formula for the depth-averaged diffusivity can be derived from the C2E Profile by integrating equation (7d) ($d_\mathrm{b} = 0.2$ m represents the depth of the sediment bed, compare with equation (11)):

$$\bar{D}_{\mathrm{enh}} = \frac{D_{\mathrm{eff},0}}{d_\mathrm{b}}\left(\ell_\mathrm{t} + \frac{1}{a}\left(1 - e^{-a\left(d_\mathrm{b} - \ell_\mathrm{t}\right)}\right)\right) \qquad (14)$$

When optimal values of $D_{\mathrm{eff},0}$, $a$ and $\ell_\mathrm{t}$ are substituted into equation (14), the resulting depth-averaged effective diffusivity ($\bar{D}_{\mathrm{enh}} = 10^{-6.66 \pm 0.03}$ m$^2$ s$^{-1}$) is equal, within error, to the optimal diffusivity inferred from the C Profile

888 using the same dataset, and the depth-averaged diffusivity inferred from the E Profile

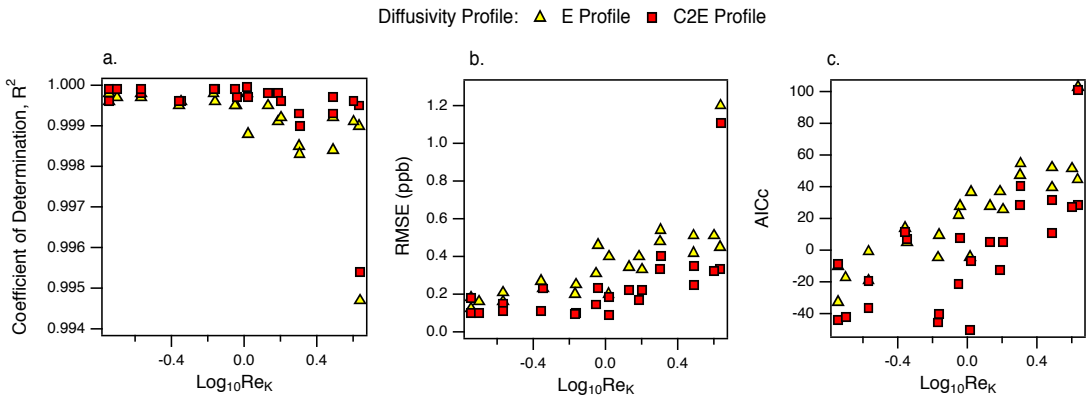


**Figure 15**. The relative performance of E and C2E Profiles across Chandler et al.'s 23 experiments. Model performance metrics include the (**a**) coefficient of determination, $R^2$, (**b**) Root Mean Square Error, RMSE, and (**c**) Akaike's Information Criterion, AICc.

(compare vertical black, blue, and green lines in **Figure 14**). At least for this single Chandler et al. experiment, all four diffusivity profiles trialed in this study (including the E2M Profile, which is indistinguishable from the E Profile, see **Section 5.5**) yield consistent estimates for the depth-averaged effective diffusivity.

### 6.2 Performance of the E and C2E Profiles across all Chandler et al. Experiments

From the single experiment analyzed in the last section we concluded that the C2E Profile is an improvement over the E Profile. This conclusion extends to the rest of Chandler et al.'s 23 experiments as well (**Figure 15** and **Tables S4** – **S7**). However, the performance gains achieved by replacing the E Profile with the C2E Profile (**Figure 15**) are relatively marginal compared to gains achieved when the C Profile was replaced with the E Profile (**Figure 11**). Both E and C2E Profile models exhibit performance loss at large Permeability Reynolds Numbers; i.e., the coefficient of determination drops, and both RMSE and AICc increase, with increasing Permeability Reynolds Number in the turbulent range (**Figures 15a, b, c**). Therefore, it appears that the loss in performance at large Permeability Reynolds

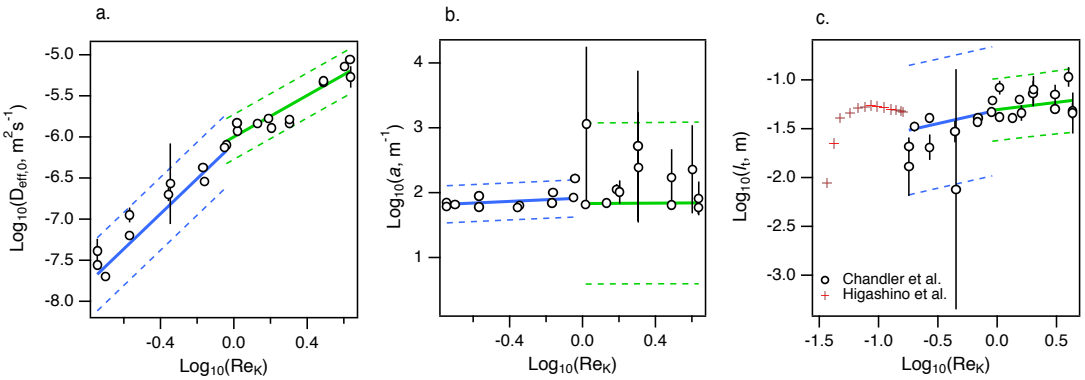


**Figure 16**. Permeability Reynolds Number scaling of the C2E Profile's three parameters: (**a**) surficial effective diffusivity; (**b**) inverse decay-length scale; and (**c**) enhanced mixing thickness. Red crosses in (c) were generated by the Higashino et al.'s pressure pulse model (details in text).

Number observed for the E Profile (**Figure 11**) cannot be resolved simply by incorporating enhanced mixing into the surficial portion of the sediment bed. An alternative hypothesis, consistent with all of our observations, is that Fick's First law (equations (1) and (2b)) is an imperfect descriptor of mass transfer in the sediment bed at large Permeability Reynolds Numbers. Notwithstanding this potential limitation, the E and C2E Profile models still capture a remarkable fraction (>99.4%) of the variance in measured water column tracer concentrations, even at the largest Permeability Reynolds Number represented in Chandler et al.'s dataset (**Figure 15a**).

### 6.3 Permeability Reynolds Number Scaling Relationships

Across all 23 of Chandler et al.'s experiments, the surficial effective diffusivity exhibits distinct Permeability Reynolds Number scaling relationships in the dispersive ($\mathrm{Re}_K < 1$) and turbulent diffusion ($\mathrm{Re}_K > 1$) ranges (based on non-overlapping 95% CIs for the slopes in equation (15a), see blue and green lines in **Figure 16a**).

$$\log_{10}\left(D_{\text{eff},0},\ \text{m}^2\text{s}^{-1}\right)=\begin{cases}\left(-6.08\pm0.03\right)+\left(2.14\pm0.06\right)\times\log_{10}\text{Re}_K,\ R^2=0.861,\ \text{Re}_K<1\\ \left(-6.00\pm0.02\right)+\left(1.26\pm0.06\right)\times\log_{10}\text{Re}_K,\ R^2=0.671,\ \text{Re}_K>1\end{cases} \quad (15a)$$

Separate scaling relationships are not indicated for the inverse depth-scale and enhanced mixing thickness (as evidenced by overlapping 95% CIs for the slopes in equations (15b) and (15c), see blue and green lines in **Figures 16b** and **16c**).

$$\log_{10}\left(a,\ \text{m}^{-1}\right)=\begin{cases}\left(1.92\pm0.04\right)+\left(0.13\pm0.08\right)\times\log_{10}\text{Re}_K,\ R^2=0.07,\ \text{Re}_K<1\\ \left(1.83\pm0.04\right)+\left(0.014\pm0.21\right)\times\log_{10}\text{Re}_K,\ R^2=0.002,\ \text{Re}_K>1\end{cases} \quad (15b)$$

$$\log_{10}\left(\ell_t,\ \text{m}\right)=\begin{cases}\left(-1.35\pm0.04\right)+\left(0.19\pm0.12\right)\times\log_{10}\text{Re}_K,\ R^2=0.06,\ \text{Re}_K<1\\ \left(-1.31\pm0.03\right)+\left(0.15\pm0.16\right)\times\log_{10}\text{Re}_K,\ R^2=0.08,\ \text{Re}_K>1\end{cases} \quad (15c)$$

When the inverse depth-scale is regressed against the pooled dataset, we find that it is roughly constant across all 23 of Chandler et al.'s experiments ($a=10^{2.03\pm0.33}$ m$^{-1}$ which corresponds to $a=140\pm130$ m$^{-1}$ after applying equations (9a) and (9b)). Repeating this exercise for the enhanced mixing thickness reveals a weak dependence of $\ell_t$ on the Permeability Reynolds Number ($\ell_t \propto \text{Re}_K^{1/4}$) across all 23 of Chandler et al.'s experiments:

$$\log_{10}\left(\ell_t,\ \text{m}\right)=\left(-1.33\pm0.02\right)+\left(0.23\pm0.06\right)\times\log_{10}\text{Re}_K,\ R^2=0.16 \quad (15d)$$

The latter scaling relationship for the enhanced mixing thickness $\ell_t$ can be compared to Higashino et al.'s turbulent pumping simulations (see discussion in **Section 6.1**) by adopting, as a proxy of the surficial portion of the sediment bed where turbulent pumping is active, the depth above which RMS vertical pore velocities are all greater than $10^{-7}$ m s$^{-1}$. This particular velocity threshold was selected because, according to Higashino et al., it occurs about 5 cm below the SWI for conditions ($u_*=0.01$ to $0.016$ m s$^{-1}$, $K=10^{-10}$ m$^2$, see their Figure 6a) similar to Chandler et al.'s experiments at the low-end of

935 the Permeability Reynolds Number range (e.g., the inferred depth of turbulence influence
936 is $\ell_t \approx 3$ cm for Exp ID 20110809, for which $u_* = 0.015$ m s$^{-1}$ and $K = 1.7 \times 10^{-10}$ m$^2$, see
937 **Tables S1** and **S7**). Higashino et al. found that both the shear velocity and sediment
938 permeability influenced the depth at which this threshold RMS vertical pore velocity
939 appears. When their simulations are recast in terms of the Permeability Reynolds Number,
940 we find that the threshold RMS vertical pore velocity shallows abruptly for Permeability
941 Reynolds Numbers less than 0.05 ($\mathrm{Re}_K < 10^{-1.3}$) (red crosses in **Figure 16c**), consistent
942 with Voerman et al.'s prediction that molecular diffusion dominates mixing across the SWI
943 when $\mathrm{Re}_K < 0.01$ (Voermans et al., 2018). Unfortunately, Higashino et al.'s simulations
944 and Chandler et al.'s experiments overlap only near the top and bottom ends of their
945 respective Permeability Reynolds Number ranges, and therefore these two datasets cannot
946 be compared directly. Nevertheless, it is interesting to note that the depth of Higashino et
947 al.'s threshold RMS vertical pore velocity flattens out around 5 cm for Permeability
948 Reynolds Numbers greater than $\mathrm{Re}_K > 10^{-1}$, consistent with observation that $\ell_t$ depends
949 weakly on $\mathrm{Re}_K$ in this range ($\ell_t \propto \mathrm{Re}_K^{1/4}$, equation (15d)).

950 **7. Application of Duhamel's Theorem to an Open System**

951 The results presented above support our central hypothesis that—by explicitly accounting
952 for depth-varying diffusivity, the change in porosity across the SWI, and two-way feedback
953 across the SWI—the evolution of solute concentration in the benthic biolayer can be
954 inferred from solute measurements in the water column. In this final section we
955 demonstrate the application of this framework to an open system of environmental
956 relevance.

## 7.1 Breakthrough of a Solute Initially Present in the Sediment Bed

Consider the common situation where interstitial fluids of an aquatic sediment are contaminated with a solute of public health or ecological concern (Weidhaas et al., 2016). As solute mixes out of the benthic biolayer and into the overlying water column, we would like to know: (1) how long must we wait for the concentration in the water column to peak? (2) what is that peak concentration? and (3) how long do we have to wait for the water column concentration to fall below some threshold value, say 0.1% of the original interstitial sediment concentration?

To address these questions, we simulated an open version of Chandler et al.'s experiment ID 20110405 (analyzed in detail in **Sections 4.1**, **5.1** and **6.1**). The simulations were run for turnover times (defined as tank volume divided by volumetric flow rate through the tank, see **Section 2.3**) ranging from $T = 10^3$ to $10^6$ s (roughly 17 minutes to 12 days). For each turnover time, we simulated a timeseries of solute concentration in the water column, given different choices of the diffusivity depth profile (C, E, and C2E) with or without two-way feedback. These six model combinations were constructed by substituting the auxiliary function solutions for the C Profile (equation (T2-2)), E Profile (equation (T2-3)), or C2E Profile (equation (T2-6b)) into the mass balance solutions for a well-mixed flow-through system with (equation (T1-5)) or without (equation (T1-7)) two-way feedback. Parameter values for the C, E, and C2E Profiles were all inferred from Exp ID 20110405 (see **Figures 3a**, **6a**, and **6b**).

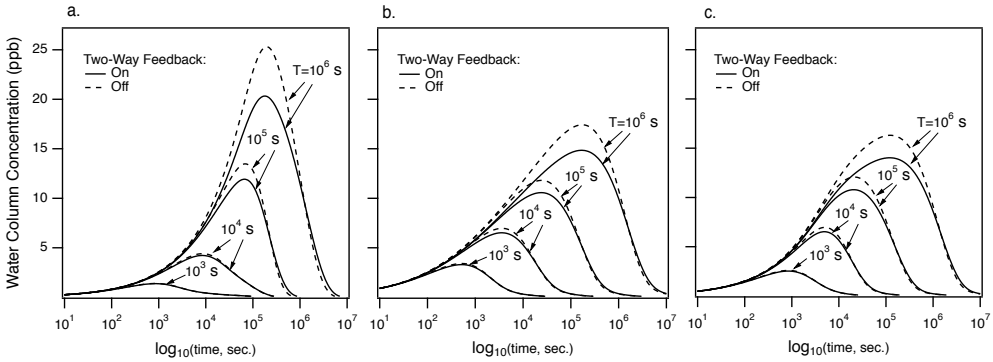


**Figure 17**. Water column breakthrough curves for a conservative tracer initially present only in the sediment bed of a well-mixed flow-through system, given four different choices of turnover times, ranging from $T = 10^3$ to $10^6$ seconds. Simulations were carried out with two-way feedback turned "on" (solid curves) or "off" (dashed curves) and for three choices of the diffusivity depth profile: (**a**) C Profile, (**b**) E Profile, or (**c**) C2E Profile. The initial solute concentration in the interstitial fluids of the sediment bed is 100 ppb, and diffusivity parameters, water column height, sediment bed depth, sediment bed porosity are consistent with Exp ID 20110405 (**Tables S1**, **S2**, **S4,** and **S7**).

## 7.2 Simulation Results

As solute mixes out of the streambed, its concentration in the water column increases with time, passes through a maximum value, and then decays with time. All three features of the solute breakthrough curve are sensitive to the turnover time $T$ of water flowing through the tank, choice of diffusivity profile (C, E, or C2E), and whether two-way feedback is turned "on" or "off" (**Figures 17** and **18**). When simulations are run with the C Profile and two-way feedback is turned on (**Figure 17a**, and black solid curves in **Figures 18a,b,c**), the peak concentration and peak arrival time increase 10-fold (from 1.4 to 20 ppb) and over 100-fold (from $10^{2.9}$ to $10^{5.3}$ s), respectively, as turnover time is increased from $T = 10^3$s (~17 minutes) to $T = 10^6$s (~12 days), for example due to declining flow through the tank

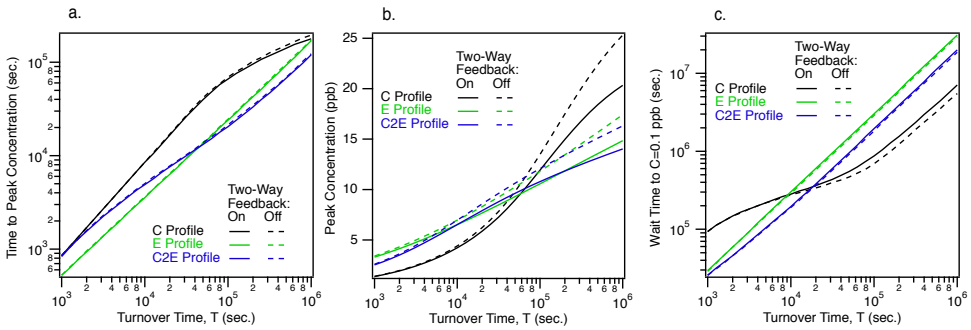


**Figure 18**. Key statistics for the breakthrough curves shown in **Figure 17**, including: (**a**) time to peak concentration, (**b**) peak concentration, and (**c**) wait time before the water column concentration falls below 0.1 ppb. Simulations were carried out with two-way feedback turned "on" (solid curves) or "off" (dashed curves) and for three choices of the diffusivity depth profile: C Profile (black curves), E Profile (green curves), or C2E Profile (blue curves). The initial solute concentration in the interstitial fluids of the sediment bed is 100 ppb, and diffusivity parameters, water column height, sediment bed depth, sediment bed porosity are consistent with Exp ID 20110405 (**Tables S1**, **S2**, **S4,** and **S7**).

(see equation (6c) and discussion thereof). This behavior is a residence time effect—decreasing the turnover time shortens the time solutes can accumulate in the tank before being "washed out" resulting in lower peak concentrations and shorter peak arrival times. Turning off two-way feedback has little influence on the C Profile's peak arrival time, but it does increase the predicted peak concentration and shorten the tail of the breakthrough curve (i.e., reduces the time needed for the concentration to fall below some threshold). When turnover time is small ($T < 10^4$ s), C Profile breakthrough curves simulated with and without two-way feedback overlap. When turnover time is large ($T > 10^4$ s), C Profile breakthrough curves simulated without two-way feedback have higher peak concentrations, shorter wait times, but similar times to peak concentration (compare dashed and solid black curves, **Figure 18**).

998 Changing the diffusivity profile alters the peak concentration, peak arrival time,
999 and wait time—but the direction (increasing or decreasing) and magnitude of these
1000 changes are case specific. For example, depending on the turnover time, replacing the C
1001 Profile with either E or C2E Profiles increases ($T < 5\times10^4$ s) or decreases ($T > 5\times10^4$ s) the
1002 peak solute concentration in the water column (**Figure 18b**). Likewise, replacing the C
1003 Profile with either E or C2E Profiles decreases ($T < 2\times10^4$ s) or increases ($T > 2\times10^4$ s) the
1004 wait time for solute concentration in the water column to fall below 0.1 ppb (**Figure 18c**).
1005 Changing the E Profile to a C2E Profile increases ($T < 2\times10^4$ s) or decreases ($T > 2\times10^4$ s)
1006 the time to peak concentration (**Figure 18a**) and decreases the wait time for the solute
1007 concentration in the water column to fall below 0.1 ppb (**Figure 18c**). On the other hand,
1008 the E and C2E Profiles have nearly identical peak solute concentrations across the full
1009 range of turnover times (**Figure 18b**). Similar to the results noted above for the C Profile,
1010 when two-way feedback is turned off and turnover time is long ($T > 10^4$ s), the E and C2E
1011 Profiles predict higher peak concentrations and shorter wait times, but similar times to
1012 peak concentration (compare dashed and solid green and blue curves, **Figure 18**). When
1013 the turnover time is short ($T < 10^4$ s), turning off two-way feedback has no effect on time
1014 to peak concentration, peak concentration, or the wait time.

1015 Given that all three profiles trialed here were optimized with the same dataset
1016 (Chandler et al.'s Exp ID 20110405) and all have (within error) the same depth-averaged
1017 diffusivity (see **Figure 15** and discussion thereof), it is perhaps surprising to learn that our
1018 solute breakthrough statistics depend, in general, on the choice of diffusivity profile. The
1019 obvious explanation is that mixing across the SWI is determined not only by the overall
1020 mixing intensity (e.g., as measured by the depth-averaged diffusivity) but also by how that

1021 mixing intensity is distributed vertically through the sediment column. Put simply, the
1022 *vertical structure* of turbulent mixing in the streambed is, all else being equal, an important
1023 control on water quality in the overlying stream.

1024 Another important lesson from these simulations is that two-way feedback impacts
1025 mass transfer across the SWI not only in closed systems (where it is responsible for the
1026 rapid deceleration of mass transfer across the SWI evident in Chandler et al.'s experiments,
1027 see our **Figures 3**, **6**, and **14**), but also in open systems, provided that the turnover times
1028 are not too short. Referring to **Figures 17** and **18**, when turnover times are long ($T > 10^4$ s)
1029 ignoring two-way feedback leads to an overestimation of the mass transfer rate across the
1030 SWI, an overestimation of the peak water column concentration, and an underestimation
1031 of the wait time required before the water column concentration falls below some threshold
1032 value. On the other hand, when when tunover times are short ($T < 10^4$ s), two-way feedback
1033 has no apparent impact on solute breakthrough statistics.

1034 **8. Conclusions and Future Research**

1035 In this paper we developed and tested a one-dimensional modeling framework, based on
1036 Duhamel's Theorem, for predicting mass transfer across the SWI and in the benthic
1037 biolayer of a turbulent stream. The framework allows for depth-varying diffusivity profiles,
1038 accounts for the change in porosity across the SWI, and encodes the two-way feedback
1039 intrinsic to these systems.

1040 We applied this new analytical framework to an extensive set of previously
1041 published measurements of turbulent mixing across a flat sediment bed in a closed stirred
1042 tank (Chandler et al., 2016), with the goal of evaluating the relative performance of four
1043 diffusivity depth profiles (C, E, E2M, and C2E Profiles, **Figure 2**). Key findings include:

- Our modeling framework is self-consistent within and across the four diffusivity depth profiles; i.e., parameter values inferred from water and sediment column measurements agree closely, and all four profiles yield similar depth-averaged diffusivities. Thus, the evolution of porewater concentrations in the benthic biolayer can be inferred from water column measurements alone, *provided that the depth-dependence and physical scaling behavior of the diffusivity profile are correctly specified*.
- For Chandler et al.'s flat-bed experiments, the diffusivity profiles scale solely as a function of the Permeability Reynolds Number, a dimensionless number that incorporates the bed shear stress and permeability of bottom sediments (both of which were varied in Chandler et al.'s experiments). The influence of bedforms on the scaling behavior of the diffusivity profiles remains to be determined.
- Replacing the C Profile with the E Profile dramatically improves all three measures of model performance, including coefficient of determination, RMSE, and AICc.
- Replacing the E Profile with the C2E Profile also improves model performance, but the gains are less dramatic (compared to replacing the C Profile with the E Profile).
- Including molecular diffusion as a lower bound on the effective diffusivity (i.e., replacing the E Profile with the E2M Profile) does not improve model performance nor change the inferred diffusivity profile parameters, at least for the range of Permeability Reynolds Numbers interrogated here ($0.2 \leq \mathrm{Re}_K \leq 4.31$). The E2M Profile may be applicable in systems with very low Permeability Reynolds Numbers.
- Performance of the E and C2E Profile models degrades for larger Permeability Reynolds Numbers, perhaps signaling that Fick's First Law is an imperfect descriptor of mass transfer across the SWI in the turbulent range ($\mathrm{Re}_K > 1$).

1067 • Notwithstanding this potential limitation of Fick's First Law, it is notable that the E
1068 and C2E Profile models capture a remarkable fraction of the variance (>99.4%) in
1069 measured water column tracer concentrations, even at the highest Permeability
1070 Reynolds Numbers trialed here.

1071 • Consistent with previous reports, we find that effective diffusivities inferred from the
1072 C Profile increase with the square of the Permeability Reynolds Number ( $D_{\mathrm{eff},0} \propto \mathrm{Re}_K^2$ ).

1073 • Effective diffusivities inferred from the E and C2E Profiles, on the other hand, exhibit
1074 different scaling behavior in the dispersion ( $D_{\mathrm{eff},0} \propto \mathrm{Re}_K^{2.4\pm0.36}$ and $D_{\mathrm{eff},0} \propto \mathrm{Re}_K^{2.14\pm0.06}$ ,
1075 $\mathrm{Re}_K < 1$ ) and turbulent diffusion ( $D_{\mathrm{eff},0} \propto \mathrm{Re}_K^{0.99\pm0.15}$ and $D_{\mathrm{eff},0} \propto \mathrm{Re}_K^{1.26\pm0.06}$, $\mathrm{Re}_K > 1$ ) ranges.

1076 • Inverse depth-scales inferred from the E Profile are constant in the dispersion range
1077 ( $a = 54 \pm 1.2\ \mathrm{m}^{-1}$, $\mathrm{Re}_K < 1$ ) and weakly decline with the Permeability Reynolds Number
1078 in the turbulent diffusion range ( $a \propto \mathrm{Re}_K^{-0.32\pm0.08}$, $\mathrm{Re}_K > 1$ ).

1079 • Inverse depth-scales inferred from the C2E Profile are constant ( $a = 140 \pm 130\ \mathrm{m}^{-1}$ )
1080 across all Permeability Reynolds Numbers investigated.

1081 • The C2E Profile's enhanced mixing thickness $\ell_t$ ranges between 1 to 10 cm and
1082 increases weakly with the Permeability Reynolds Number ( $\ell_t \propto \mathrm{Re}_K^{1/4}$ ), consistent with
1083 a previously published model for mixing in the surficial portion of the streambed by
1084 turbulent pumping (Higashino et al., 2009).

1085 • Interestingly, the $1/e$-folding depth inferred from the E and E2M Profiles also increases,
1086 from about 1.5 to 6.6 cm, with increasing Permeability Reynolds Number, suggesting
1087 that both $\ell_t$ (C2E Profile) and $1/a$ (E and E2M Profile) represent the thickness of the
1088 surficial portion of the bed vigorously mixed by turbulent pumping.

- Given the concordance between these mixing depth-scales (1 to 10 cm) and the depth of the benthic biolayer (< 10 cm), turbulent pumping may dominate hyporheic exchange within the benthic biolayer of flat streambeds.
- The influence of turbulent pumping (and likely other turbulence-driven mechanisms of hyporheic exchange) diminishes rapidly for Permeability Reynolds Numbers less than 0.04 (see **Figure 16c**). For this range of the Permeability Reynolds Number, mixing in the benthic biolayer is likely to be dominated by molecular diffusion.
- Extension of our analytical framework to an open system (in which the solute is initially present in the sediment bed) reveals that key solute breakthrough statistics (e.g., arrival time of the solute peak, peak solute concentration, and the wait time for the concentration to fall below a critical threshold) are all influenced by the nature of the diffusivity profile (C, E, or C2E) and whether or not two-way feedback is considered.
- Two-way feedback is particularly important in closed systems, and in open systems characterized by long turnover times.

Moving forward, we can identify a number of promising avenues for future research, including: (1) extending our framework to include non-conservative solutes, with the long-term goal of evaluating, and predicting, how mixing and non-conservative processes in the benthic biolayer (reaction, adsorption, absorption) collectively regulate stream water quality; (2) exploring how bedforms, such as ripples and dunes, alter our results, for example by changing the Permeability Reynolds Number scaling of diffusivity profile parameters; (3) more generally, evaluating how well the scaling relationships developed here translate to conditions more representative of the turbulent velocity boundary layer in streams; (4) exploring the influence of polydisperse sediments; (5) investigating links

between depth-varying nutrient transport and biologically induced heterogeneity in sediment permeability (Caruso et al., 2017); and (6) incorporating our modeling framework into catchment-to-continental scale river network models (Schmadel et al., 2019; Gomez-Velez et al., 2015; Gomez-Velez and Harvey, 2014).

## Acknowledgments and Data

The authors declare no conflicts of interest. All data used in this study are publicly available (www.doi.org/10.15131/shef.data.10120205). SBG was supported by the U.S. National Science Foundation (award 1840504), Virginia Tech's ICTAS EFO Opportunity Seed Investment Grant, and the UC Office of the President Multi-campus Research Program Initiative award (MRP-17-455083). JGV was funded by the U.S. National Science Foundation (award EAR 1830172) and the U.S. Department of Energy, Office of Biological and Environmental Research (BER), as part of BER's Subsurface Biogeochemistry Research Program (SBR). This contribution originates from the SBR Scientific Focus Area (SFA) at the Pacific Northwest National Laboratory (PNNL). IG was supported by UK EPSRC Established Career Fellowship (award EP/P012027/1). MG was funded by the Australian Research Council's Discovery Projects funding scheme (DP120102500). KRR was supported by a fellowship from the Fulbright Program. JH was supported by the USGS Water Resources Availability Program. The authors thank M. Chappell and A. Monofy for their insightful comments and manuscript edits.

**Appendix A. Duhamel's Theorem for Spatially Variable Diffusion Coefficients.** In this appendix we demonstrate that Duhamel's convolution integral (equation (5a)) satisfies the reduced form of the diffusion equation (equation (2c)) and associated initial (equation (3a) and boundary conditions (equation (3b) and either equation (3e) or (3f)) for any choice of the spatially varying diffusivity profile function $f\left(\overline{x}\right)$. Specifically, we aim to demonstrate that equation (A1) satisfies a rearranged version of the reduced diffusion equation (equation (A2a)), the initial condition (equation (A2b)), the upper boundary condition (equation (A2c)), and two possible lower boundary conditions (a Dirichlet boundary condition for an infinitely deep bed, or a no-flux equations for a finite bed, equations (A2d) or (A2e), respectively):

$$u\left(\overline{x},\overline{t}\right)=\int_0^{\overline{t}}U\left(\overline{x},\overline{t}-v\right)\frac{dF}{dv}dv+U\left(\overline{x},\overline{t}\right) \tag{A1}$$

$$\frac{\partial u}{\partial \overline{t}}-\frac{\partial}{\partial \overline{x}}\left(f\left(\overline{x}\right)\frac{\partial u}{\partial \overline{x}}\right)=0 \tag{A2a}$$

$$u\left(\overline{x},\overline{t}=0\right)=0 \tag{A2b}$$

$$u\left(\overline{x}=0,\overline{t}\right)=F\left(\overline{t}\right)H\left(\overline{t}\right)\overset{\overline{t}>0}{=}F\left(\overline{t}\right) \tag{A2c}$$

$$u\left(\overline{x}\to\infty,\overline{t}\right)=0 \tag{A2d}$$

$$\left.\frac{\partial u}{\partial \overline{x}}\right|_{\overline{x}=\overline{d}_b}=0 \tag{A2e}$$

We begin by demonstrating that equation (A1) satisfies equation (A2a). Taking the time derivative of equation (A1) and applying Leibnitz' rule, we obtain:

$$\frac{\partial u}{\partial \overline{t}}=U\left(\overline{x},0\right)\frac{dF}{d\overline{t}}+\int_0^{\overline{t}}\frac{\partial}{\partial \overline{t}}\left[U\left(\overline{x},\overline{t}-v\right)\right]\frac{dF}{dv}dv+\frac{\partial U}{\partial \overline{t}}=\int_0^{\overline{t}}\frac{\partial}{\partial \overline{t}}\left[U\left(\overline{x},\overline{t}-v\right)\right]\frac{dF}{dv}dv+\frac{\partial U}{\partial \overline{t}} \tag{A3}$$

1151 The second equal sign follows from the requirement that the auxiliary solution satisfy the

1152 initial condition, $U\left(\bar{x},0\right)=0$ (see equation (5c)). Substituting equation (A1) into the second

1153 term on the left-hand side of equation (A2a) we also obtain:

1154 $$\frac{\partial}{\partial\bar{x}}\left[f\left(\bar{x}\right)\frac{\partial u}{\partial\bar{x}}\right]=\int_0^{\bar{t}}\frac{\partial}{\partial\bar{x}}\left[f\left(\bar{x}\right)\frac{\partial}{\partial\bar{x}}\left[U\left(\bar{x},\bar{t}-v\right)\right]\right]\frac{dF}{dv}dv+\frac{\partial}{\partial\bar{x}}\left[f\left(\bar{x}\right)\frac{\partial U}{\partial\bar{x}}\right] \tag{A4}$$

1155 Substituting equations (A3) and (A4) into equation (A2a) we arrive at equation (A5),

1156 where the new variable $\bar{t}'$ is defined as follows, $\bar{t}'=\bar{t}-v>0$:

1157 $$\frac{\partial u}{\partial\bar{t}}-\frac{\partial}{\partial\bar{x}}\left[f\left(\bar{x}\right)\frac{\partial u}{\partial\bar{x}}\right]=\int_0^{\bar{t}}\left\{\frac{\partial U}{\partial\bar{t}'}-\frac{\partial}{\partial\bar{x}}\left[f\left(\bar{x}\right)\frac{\partial}{\partial\bar{x}}U\left(\bar{x},\bar{t}'\right)\right]\right\}\frac{dF}{dv}dv+\left\{\frac{\partial U}{\partial\bar{t}}-\frac{\partial}{\partial\bar{x}}\left[f\left(\bar{x}\right)\frac{\partial}{\partial\bar{x}}U\left(\bar{x},\bar{t}\right)\right]\right\} \tag{A5}$$

1158 By definition, the auxiliary function $U$ satisfies equation (5b), and therefore the differential

1159 equations appearing inside the two curly brackets on the right hand side of equation (A5)

1160 are identically equal to zero. This implies that the right hand side of equation (A5) is also

1161 identifically equal to zero, and therefore equation (A2a) is satisfied for any choice of the

1162 diffusivity profile function, $f\left(\bar{x}\right)$. Equation (A1) also satisfies the initial condition

1163 (equation (A2b)), where the second equal sign follows from the initial condition imposed

1164 on the auxiliary function solution (see equation (5c)):

1165 $$u\left(\bar{x},\bar{t}=0\right)=U\left(\bar{x},\bar{t}=0\right)=0 \tag{A6}$$

1166 Equation (A1) also satisfies the upper boundary condition (equation (A2c)), where we

1167 have used the fact that, by definition, $F\left(0\right)=1$ (equation (3c)) and $U\left(\bar{x}=0,\bar{t}\right)=1$ for $\bar{t}>0$

1168 (equation (5d)):

1169 $$u\left(\bar{x}=0,\bar{t}\right)=\int_0^{\bar{t}}U\left(0,\bar{t}-v\right)\frac{dF}{dv}dv+U\left(0,\bar{t}\right)=F\left(\bar{t}\right)-F\left(0\right)+1=F\left(\bar{t}\right),\ \bar{t}>0$$

1170 Finally, equation (A1) satisfies both lower boundary conditions considered in this study
1171 (equations (A2d) and (A2e)). The former is satisfied because, for an infinitely deep bed we
1172 require that the auxiliary function obey the limit, $U\left(\overline{x}\to\infty\right)=0$ (see equation (5e)):

1173 $$u\left(\overline{x}\to\infty,\overline{t}\right)=\lim_{\overline{x}\to\infty}\left[\int_0^{\overline{t}}U\left(\overline{x},\overline{t}-v\right)\frac{dF}{dv}dv+U\left(\overline{x},\overline{t}\right)\right]=\int_0^{\overline{t}}U\left(\overline{x}\to\infty,\overline{t}-v\right)\frac{dF}{dv}dv+U\left(\overline{x}\to\infty,\overline{t}\right)=0$$

1174 The latter is satisfied because, for a finite bed, we require that the auxiliary function obey
1175 the no-flux boundary condition at the base of the sediment bed, $\left(\partial U/\partial\overline{x}\right)_{\overline{x}=\overline{d}_b}=0$ (equation
1176 (5f)).

1177 $$\left.\frac{\partial u}{\partial\overline{x}}\right|_{\overline{x}=\overline{d}_b}=\int_0^{\overline{t}}\frac{\partial}{\partial\overline{x}}\left[U\left(\overline{x}=\overline{d}_b,\overline{t}-v\right)\right]\frac{dF}{dv}dv+\left.\frac{\partial U}{\partial\overline{x}}\right|_{\overline{x}=\overline{d}_b}=0$$

1178 **Appendix B. Derivation of Solutions for the Evolution of Solute Concentrations in**
1179 **the Water and Sediment Columns of a Closed System.** In this appendix we derive
1180 expressions for the solute concentration above and below the SWI in a closed system
1181 accounting for two-way feedback. This requires coupling the water column mass balance
1182 equation for a closed system (equation (6a)) to the sediment column mass balance equation
1183 (equation (2c) and associated boundary and initial conditions). We accomplish this by
1184 invoking Duhamel's Theorem (see equation (5a) in the main text):

1185 $$u\left(\overline{x},\overline{t}\right)=\int_0^{\overline{t}}U\left(\overline{x},\overline{t}-v\right)\frac{d}{dv}\left[F\left(v\right)H\left(v\right)\right]dv=\int_0^{\overline{t}}U\left(\overline{x},\overline{t}-v\right)\frac{dF}{dv}dv+U\left(\overline{x},\overline{t}\right)\qquad\text{(B1)}$$

1186 The second equal sign follows by applying the product rule to the derivative in the
1187 integrand, equating the derivative of the Heaviside function to the Dirac Delta function,
1188 invoking the commutative property of the convolution integral, and applying the combing
1189 property of the Dirac Delta. The rest of the derivation is simplified if we move from the
1190 time domain to the Laplace domain, in part because the convolution of two variables in the

1191 former is their product in the latter (Graff, 2004). In the Laplace domain, Duhamel's
1192 convolution integral (equation (B1)) simplifies dramatically; note that we have used the
1193 fact that the forcing function's initial condition is $F\left(\bar{t}=0\right)=1$, see equation (3c):

1194 $$\tilde{u}\left(\bar{x},s\right)=s\tilde{U}\left(\bar{x},s\right)\tilde{F}\left(s\right) \tag{B2}$$

1195 According to equation (B2), the Laplace transform of the dependent variable ($\tilde{u}$) can be
1196 calculated from the product of the Laplace transform variable $s$, and Laplace transforms
1197 of the auxiliary function $\tilde{U}$, and of the forcing function $\tilde{F}$. As noted in the main text, the
1198 auxiliary function is obtained by solving equations (5b) through (5d), after specifying the
1199 diffusivity depth profile $f\left(\bar{x}\right)$ and the lower boundary condition (equation (5e) or (5f)). An
1200 expression for the forcing function can be derived by taking the Laplace transform of the
1201 water column mass balance (equation (4b)) and rearranging:

1202 $$\tilde{F}\left(s\right)=\frac{1}{s}\left(\frac{1}{\bar{h}_w}\left.\frac{\partial\tilde{u}}{\partial\bar{x}}\right|_{\bar{x}=0,s}+1\right) \tag{B3}$$

1203 As noted in the main text, due to the two-way feedback inherent in our system our forcing
1204 function requires knowledge of the evolving concentration field in the sediment bed (i.e.,
1205 a derivative of $\tilde{u}$ appears on the right hand side of equation (B3)). In turn, the solution for
1206 the dependent variable $\tilde{u}$ requires knowledge of the forcing function ($\tilde{F}$ appears on the
1207 right hand side of equation (B2)). To address this two-way feedback, we begin by solving
1208 for the differential term on the right hand side of equation (B3). This involves: (1)
1209 combining equations (B2) and (B3); (2) differentiating both sides with respect to $\bar{x}$; (3)
1210 evaluating the resulting expression at $\bar{x}=0$; and (4) rearranging:

1211 $$\left.\frac{\partial\tilde{u}}{\partial\bar{x}}\right|_{\bar{x}=0,s}=\frac{\left(\partial\tilde{U}/\partial\bar{x}\right)_{\bar{x}=0,s}}{1-\frac{1}{\bar{h}_w}\left(\partial\tilde{U}/\partial\bar{x}\right)_{\bar{x}=0,s}} \tag{B4}$$

A solution for the dependent variable immediately follows by combining equations (B2), (B3) and (B4):

$$\tilde{u}\left(\bar{x},s\right)=\frac{\tilde{U}\left(\bar{x},s\right)}{1-\frac{1}{\bar{h}_w}\left(\partial\tilde{U}/\partial\bar{x}\right)_{\bar{x}=0,s}} \tag{B5}$$

Taking the inverse Laplace Transform of this last result and rearranging, we obtain a solution for the evolution of the sediment column concentration (equation (T1-2) in **Table 1**). Likewise, a solution for the water column concentration can be derived by combining equations (B3) and (B4), taking the inverse Laplace Transform, and rearranging (equation (T1-1) in **Table 1**). The cumulative mass transferred from the sediment bed to the overlying water column ( $M_s\left(\bar{t}\right)$, equation (B6)) and the cumulative mass transferred into the overlying water column from the sediment bed ( $M_w\left(\bar{t}\right)$, equation (B7)) can also be derived from these results:

$$M_s\left(\bar{t}\right)=\frac{A\theta}{a}\left(C_{s0}-C_{w0}\right)\mathcal{L}^{-1}\left[\frac{\int_0^\infty\tilde{U}\left(\bar{x},s\right)d\bar{x}}{1-\frac{1}{\bar{h}_w}\left(d\tilde{U}/d\bar{x}\right)_{\bar{x}=0,s}}\right] \tag{B6}$$

$$M_w\left(\bar{t}\right)=Ah_w\left(C_{s0}-C_{w0}\right)\left(1-\mathcal{L}^{-1}\left[\frac{1/s}{1-\frac{1}{\bar{h}_w}\left(d\tilde{U}/d\bar{x}\right)_{\bar{x}=0,s}}\right]\right) \tag{B7}$$

**Appendix C. Derivation of Auxiliary Function Solutions.** In this appendix we derive Laplace domain solutions for the auxiliary function $\tilde{U}$ given four different choices of the diffusivity depth profile (C, E, E2M, and C2E, see **Section 2.5**), and two different choices of the bottom boundary condition (finite or infinite sediment bed).

*Auxiliary Functions for the C Profile*. Substituting equation (7a) into equation (5b) and taking the Laplace transform of equations (5b) through (5d), we arrive at the following

1231 ordinary differential equation and upper boundary condition for the auxiliary function
1232 where $s$ is the Laplace transform variable (the initial condition (equation (5c)) is
1233 incorporated into the Laplace transform of the differential equation):

1234 $$s\tilde{U} = \frac{d^2\tilde{U}}{d\bar{x}^2},\ \tilde{U}\left(\bar{x}=0,s\right) = \frac{1}{s} \qquad \text{(C1)}$$

1235 The Laplace Transform of the two possible lower-boundary condition (infinite or finite
1236 bed boundary conditions, equations (5e) or (5f)) are as follows:

1237 $$\tilde{U}\left(\bar{x}\to\infty,s\right)=0 \qquad \text{(C2a)}$$

1238 $$\left.\frac{\partial\tilde{U}}{\partial\bar{x}}\right|_{\bar{x}=\bar{d}_b}=0 \qquad \text{(C2b)}$$

1239 This ordinary differential equation is easily integrated, yielding two auxiliary functions
1240 for the infinite and finite sediment beds (equations (T2-1) and (T2-2) in **Table 2**).

1241 *Auxiliary Functions for the E Profile*. Substituting equation (7b) into equation
1242 (5b) we obtain the following differential equation for the auxiliary function:

1243 $$\frac{\partial U}{\partial\bar{t}} = e^{-\bar{x}}\frac{\partial^2 U}{\partial\bar{x}^2} - e^{-\bar{x}}\frac{\partial U}{\partial\bar{x}} \qquad \text{(C3)}$$

1244 Following the approach outlined by Yates (1992), equation (C3) can be simplified by a
1245 change of coordinate, $\xi = e^{\bar{x}}$:

1246 $$\frac{\partial U}{\partial\bar{t}} = \xi\frac{\partial^2 U}{\partial\xi^2},\ \xi = e^{\bar{x}},\ \bar{x}\ge 0 \qquad \text{(C4a)}$$

1247 The corresponding initial and upper boundary conditions are as follows

1248 $$U\left(\xi,\bar{t}=0\right)=0,\ \xi\ge 1 \qquad \text{(C4b)}$$

1249 $$U\left(\xi=1,\bar{t}\right)=1 \qquad \text{(C4c)}$$

1250 The corresponding lower boundary conditions for an infinite and finite are equations

1251 (C4d) and (C4e).

1252 $$U\left(\xi \to \infty, \bar{t}\right) = 0 \qquad \text{(C4d)}$$

1253 $$\left.\frac{\partial U}{\partial \xi}\right|_{\xi = e^{\vec{a}_b}} = 0 \qquad \text{(C4e)}$$

1254 Taking the Laplace transform of these equations, we arrive at the corresponding ordinary

1255 differential equation and boundary conditions:

1256 $$s\tilde{U}\left(s\right) = \xi \frac{d^2\tilde{U}}{d\xi^2},\ \xi \geq 1 \qquad \text{(C5a)}$$

1257 $$\tilde{U}\left(\xi = 1, s\right) = 1/s \qquad \text{(C5b)}$$

1258 $$\tilde{U}\left(\xi \to \infty, s\right) = 0 \qquad \text{(C4d)}$$

1259 $$\left.\frac{\partial \tilde{U}}{\partial \xi}\right|_{\xi = e^{\vec{a}_b}} = 0 \qquad \text{(C5c)}$$

1260 Solving this differential equation we arrive at a set of auxiliary functions for the infinite

1261 and finite bed cases (equations (T2-3) and (T2-4), respectively, in Table 2).

1262 *Auxiliary Function for the E2M Profile.* Let $U_1$ and $U_2$ be solutions for the

1263 auxiliary function in the upper ($0 \leq x \leq \ell_m$) and lower ($x > \ell_m$) domains of the sediment bed,

1264 where the variable $\ell_m$ represents the depth at which the diffusivity profile transitions from

1265 exponentially declining to constant and equal to the tortuosity-modified molecular

1266 diffusion coefficient (see equation (7c)). The two mass conservation equations (equations

1267 (C6a) and (C6d)), initial conditions (equations (C6b) and (C6e)), and boundary conditions

1268 (equations (C6c) and (C6f)) for the two domains are as follows:

$$\frac{\partial U_1}{\partial \overline{t}} = \frac{\partial}{\partial \overline{x}}\left[ e^{-\overline{x}} \frac{\partial U_1}{\partial \overline{x}} \right], \; 0 \le \overline{x} < \overline{\ell}_{\mathrm{m}} \tag{C6a}$$

$$U_1\left(\overline{x}, \overline{t} = 0\right) = 0 \tag{C6b}$$

$$U_1\left(\overline{x} = 0, \overline{t}\right) = 1 \tag{C6c}$$

$$\frac{\partial U_2}{\partial \overline{t}} = \overline{D} \frac{\partial^2 U_2}{\partial \overline{x}'^2}, \; \overline{x}' = \overline{x} - \overline{\ell}_{\mathrm{m}} > 0 \tag{C6d}$$

$$U_2\left(\overline{x}', \overline{t} = 0\right) = 0 \tag{C6e}$$

$$U_2\left(\overline{x}' \to \infty, \overline{t}\right) = 0 \tag{C6f}$$

For mathematical convenience, in the lower domain we have introduced a new coordinate system centered on the interface between the two domains ( $x' = x - \ell_{\mathrm{m}}$ ). Following the approach outlined by Carslaw and Jaeger (2011) for solving composite diffusion problems (see pages 319-326), two interfacial matching conditions are also required, one to ensure that the tracer concentration is equal on both sides of the interface (equation (C6g)) and the other to ensure that there is no accumulation of tracer mass at the interface (equation (C6h)).

$$U_1\left(\overline{x} = a\ell_{\mathrm{m}}, \tau\right) = U_2\left(\overline{x}' = 0, \tau\right) \tag{C6g}$$

$$\left.\frac{\partial U_1}{\partial \overline{x}}\right|_{\overline{x} = a\ell_{\mathrm{m}}} = \left.\frac{\partial U_2}{\partial \overline{x}'}\right|_{\overline{x}' = 0} \tag{C6h}$$

Taking the Laplace transform of these equations leads to a set of differential equations that are isomorphic to the E and C Profiles above. Therefore, their auxiliary solutions can be adopted here, except that the four unknown integration constants must be obtained by solving the system of algebraic equations formed when the two solutions are substituted into the two boundary conditions (corresponding to the upper and lower sediment boundaries, equations (C6c) and (C6f), and two interfacial matching conditions (equations

(C6g) and (C6f)). While the overall solution is expressed as separate auxiliary functions for the upper and lower-domains (equations (T2-5b) and (T2-5c) in Table 2) it is important to note that, by virtue of the interfacial conditions (equations (C6g) and (C6f)), the evolution of tracer concentration in the lower domain influences the evolution of tracer concentration in the upper domain, and vice versa. Indeed, when these solutions are coupled to tracer concentration in the water column through Duhamel's Theorem (the overall system encodes multiple two-way feedbacks, between tracer concentrations in the upper and lower domains of the sediment bed, and between tracer concentrations in the sediment bed and the overlying water column.

*Auxiliary Function for the C2E Profile*. Let $U_1$ and $U_2$ represent the auxiliary functions in the upper ( $x \le \ell_t$ ) and lower ( $x > \ell_t$ ) domains of the sediment bed, where $x = \ell_t$ represents the depth at which the diffusivity profile transitions from constant (equal to the surface diffusivity $D_{\text{eff},0}$ ) to exponentially declining (equation (7d)). The two mass conservation equations (equations (C7a) and (C7d)), initial conditions (equations (C7b) and (C7e)), and boundary conditions (equations (C7c) and (C7f)), and interfacial conditions (equations (C7g) and (C7f)) for the two domains are as follows:

$$\frac{\partial U_1}{\partial \overline{t}} = \frac{\partial^2 U_1}{\partial \overline{x}'^2}, \; -\overline{\ell}_t < \overline{x}' < 0 \tag{C7a}$$

$$U_1\left(\overline{x}', \overline{t} = 0\right) = 0 \tag{C7b}$$

$$U_1\left(\overline{x}' = -\ell_t a, \overline{t}\right) = 1 \tag{C7c}$$

$$\frac{\partial U_2}{\partial \overline{t}} = \frac{\partial}{\partial \overline{x}'}\left[ e^{-\overline{x}'} \frac{\partial U_2}{\partial \overline{x}'} \right], \; \overline{x}' > 0 \tag{C7d}$$

$$U_2\left(\overline{x}', \overline{t} = 0\right) = 0 \tag{C7e}$$

$$U_2\left(\overline{x}' \to \infty, \overline{t}\right) = 0 \tag{C7f}$$

$$U_1\left(\overline{x}' = 0, \overline{t}\right) = U_2\left(\overline{x}' = 0, \overline{t}\right) \tag{C7g}$$

$$\left.\frac{\partial U_1}{\partial \overline{x}}\right|_{\overline{x}'=0} = \left.\frac{\partial U_2}{\partial \overline{x}'}\right|_{\overline{x}'=0} \tag{C7h}$$

For convenience, we have centered the depth coordinate for both auxiliary functions (equations (C7a) and (C7d)) on the interface between the two domains ($x' = x - \ell_{\mathrm{m}}$). Following the procedure outlined above for the E2M profile, we arrive at Laplace-domain solutions for the auxiliary solutions for $U_1$ and $U_2$ are summarized in **Table 2** (equations (T2-6b) and (T2-6c)).

**References.**


Ang, A.H.S. & Tang, W.H. (2007), "Probability Concepts in Engineering: Emphasis on Applications to Civil and Environmental Engineering", Hoboken NJ, John Wiley & Sons, 2nd Ed.

Anim, D.O., Fletcher, T.D., Vietz, G.J., Burns, M.J., & Pasternack, G.B. (2019), How alternative urban stream channel designs influence ecohydraulic conditions. *J. Environmental Management*, 247, 242-252. https//doi:10.1016/j.jenvman.2019.06.095

Aho, K., Derryberry, D., & Peterson, T. (2014), Model selection for ecologists: the worldviews of AIC and BIC. *Ecology*, 95(3), 631-636. https//doi:10.1890/13-1452.1

Azizian, M., Boano, F., Cook, P.L.M., Detwiler, R.L., Rippy, M.A., & Grant, S.B. (2017), Ambient groundwater flow diminishes nitrate processing in the hyporheic zone of streams, *Water Resources Research*, 53, doi:10.1002/2016WR020048.

Battin, T. J., Kaplan, L. A., Findlay, S., Hopkinson, C. S., Martí, E., Packman, A. I., et al. (2008), Biophysical controls on organic carbon fluxes in fluvial networks. *Nature Geoscience*, 1(2), 95–100. https//doi:10.1038/ngeo101

Bhaskar, A.S., Harvey, J.W., Henry, E.J. (2012), Resolving hyporheic and groundwater components of streambed water flux using heat as a tracer. *Water Resources Research*, 48, W08524. doi:10.1029/2011WR011784

Boano, F., Harvey, J. W., Marion, A., Packman, A. I., Revelli, R., Ridolfi, L., & Wörman, A. (2014), Hyporheic flow and transport processes: Mechanisms, models, and biogeochemical implications. *Reviews of Geophysics*, 52, 603-679. https//doi:10.1002/2012RG000417

Boano, F., Revelli, R, & Ridolfi, L. (2011), Water and solute exchange through flat streambeds induced by large turbulent eddies. *J. Hydrol*ogy, 402, 290-296.

Bottacin-Busolin, A. (in press), Modeling the effect of hyporheic mixing on stream solute transport. *Water Resource Research*. https://doi.org/10.1029/2019WR025697

Breugem, W.P., Boersma, B.J., & Uittenbogaard, R.E. (2006) The influence of wall permeability on turbulent channel flow. *J. Fluid Mech*. 562, 35-72.

Cardenas, M., J. L. Wilson, & R. Haggerty (2008), Residence time of bedform-driven hyporheic exchange. *Advances Water Research*, 31, 1382-1386.

Caruso, A., F. Boano, L. Ridolfi, D. L. Chopp, & A. Packman (2017), Biofilm-induced bioclogging produces sharp interfaces in hyporheic flow, redox conditions, and microbial community structure, *Geophys. Res. Lett*., 44, 4917–4925, doi:10.1002/2017GL073651.

Carslaw, H.S. & J.C. Jaeger (2011) "Conduction of Heat in Solids" (Third Ed.), Oxford University Press, London, England.

Chandler, I.D. (2012), "Vertical variation in diffusion coefficient within sediments", PhD thesis, Univ of Warwick, Coventry, U.K.

1355 Chandler, I.D., Guymer, I., Pearson, J.M., & Egmond, R.V. (2016), Vertical variation of
1356 mixing within porous sediment beds below turbulent flows. *Water Resources Research*, 52,
1357 3493-3509. https://doi.org/10.1002/2015WR018274

1358 Cohn, T.A. (2005), Estimating contaminant loads in rivers: An application of adjusted
1359 maximum likelihood to type 1 censored data. *Water Resources Research*, 41, W07003.
1360 https//doi:10.1029/2004WR003833

1361 Cooper, J.R., Ockleford, A., Rice, S.P., & Powell, D.M. (2018) Does the permeability of
1362 gravel river beds affect near-bed hydrodynamics? Earth Surface Processes and Landforms,
1363 43(5), 943-955. https://doi.org/10.1002/eesp.4260

1364 Cozzarelli, I.M., Akob, D.M., Baedecker, M.J., Spencer, T., Jaeschke, J., Dunlap, D.S.,
1365 Mumford, A.C., Poret-Peterson, A.T., & Chambers, D.B. (2017) Degradation of Crude 4-
1366 MCHM (4-Methylcyclohexanemethanol) in sediments from Elk River, West Virginia.
1367 *Environmental Science and Technology*, 51, 12139-12145.

1368 Dahm, C. N., Grimm, N. B., Marmonier, P., Valett, H. M., & Vervier, P. (2002), Nutrient
1369 dynamics at the interface between surface waters and groundwaters. *Freshwater Biology*,
1370 40(3), 427–451. https//doi:10.1046/j.1365-2427.1998.00367.x

1371 Elliott, A. H., & N. H. Brooks (1997a), Transfer of nonsorbing solutes to a streambed with
1372 bed forms: Theory, *Water Resources Research*, 33, 123–136.

1373 Elliott, A. H., & N. H. Brooks (1997b), Transfer of nonsorbing solutes to a streambed with
1374 bed forms: Laboratory experiments. *Water Resources Research*, 33, 137–151.

1375 Fleckenstein, J.H., Krause, S., Hannah, D.M., Boano, F. (2010), Groundwater-surface
1376 water interactions: New methods and models to improve understanding of processes and
1377 dynamics. *Adv. Water Resources*, 33, 1291-1295.

1378 Franca, M.J. & Brocchini, M. (2015), Turbulence in Rivers. In P. Rowinski & A.
1379 Radecki-Pawlick (Eds.), *Rivers—Physical, Fluvial, and Environmental Processes,*
1380 GeoPlanet: Earth and Plaetary Sciences, doi 10.1007/978030319-17719-9_2 (pp. 51–78).
1381 Springer International Publishing, Switzerland.

1382 Garcia, M.H. (2008), Sediment transport and morphodynamics, Sediment Engineering:
1383 Processes, measurements, modeling, and practice. ASCE Manual No 110, Am. Soc. Of
1384 Civ. Eng., ISBN 10 # 0784408149. https//doi: 10.1061/40856(200)94

1385 Graff, U. (2004) "Applied Laplace Transforms and z-Transforms for Scientists and
1386 Engineers—A Computational Approach using a Mathematica Package", New York, NY,
1387 Springer-Basal AG, 1st Ed.

1388 Grant, S. B. & Marusic, I. (2011), Crossing Turbulent Boundaries: Interfacial Flux in
1389 Environmental Flows. *Environmental Science and Technology*, 45, 7107-7113.
1390 https//doi:10.1021/es201778s

1391 Grant, S. B. Stewardson, M. J. & Marusic, I. (2012), Effective diffusivity and mass flux
1392 across the sediment-water interface in streams. *Water Resources Research*, 48, W05548.
1393 https//doi:10.1029/2011WR011148

1394 Grant, S. B., Stolzenbach, K., Azizian, M., Stewardson, M. J., Boano, F., & Bardini, L.
1395 (2014), First-Order Contaminant Removal in the Hyporheic Zone of Streams: Physical

Insights from a Simple Analytical Model. *Environmental Science and Technology*, 48, 11369-11378. https//doi: 10.1021/es501694k

Grant, S. B., Azizian, M., Cook, P., Boano, F. & Rippy, M. A. (2018a), Factoring stream turbulence into global assessments of nitrogen pollution. *Science*, 359, 1266-1269. https//doi:10.1126/science.aap8074

Grant, S.B. Gomez-Velez, J.D., & Ghisalberti, M. (2018b), Modeling the effects of turbulence on hyporheic exchange and local-to-global nutrient processing in streams. *Water Resources Research*, 54, https//doi:10.1029/2018WR023078.

Gomez-Velez, J. D., & Harvey, J. W. (2014), A hydrogeomorphic river network model predicts where and why hyporheic exchange is important in large basins. *Geophysical Research Letters*, 2014GL061099. https//doi:10.1002/2014GL061099

Gomez-Velez, J. D., Harvey, J. W., Cardenas, M. B., & Kiel, B. (2015), Denitrification in the Mississippi River network controlled by flow through river bedforms. *Nature Geoscience*, 8, 941-945. https// doi:10.1038/ngeo2567

Harvey, J. W., Böhlke, J. K., Voytek, M. A., Scott, D., & Tobias, C. R. (2013), Hyporheic zone denitrification: Controls on effective reaction depth and contribution to whole-stream mass balance. *Water Resources Research*, 49(10), 6298–6316. https//doi:10.1002/wrcr.20492

Herzog, S.P., Higgins, C.P, Singha, K., & McCray, J.E. (2018), Performance of engineered streambeds for inducing hyporheic transient storage and attenuation of resazurin. *Environmental Science & Technology* 52, 10627-10636.

Hester, E. T., Cardenas, M. B., Haggerty, R., & Apte, S. V. (2017), The importance and challenge of hyporheic mixing. *Water Resources Research*, 53(5), 3565–3575. https//doi:10.1002/2016WR020005

Hester, E. T. & Gooseff, M. N. (2010), Moving beyond the banks: hyporheic restoration is fundamental to restoring ecological services and functions of streams. *Environmental Science & Technology*, 44(5), 1521-1525. https//doi:10.1021/es902988n

Higashino, M.J., Clark, J., & Stefan, H. (2009) Pore water flow due to nearbed turbulence and associated solute transfer in a stream or lake sediment bed. *Water Resources Research* 45, W12414. doi:10.1029/2008WR007374

Hill, C.G. (1977) "An Introduction to Chemical Engineering Kinetics and Reactor Design", New York, NY, John Wiley & Sons, Inc., 1st Ed.

Hondzo, M. (1998), Dissolved oxygen transfer at the sediment-water interface in a turbulent flow. *Water Resources Research,* 34(12), 3525-3533.

Iversen, N, & Jorgensen, B.B. (1993), Diffusion coefficients of sulfate and methane in marine sediments: Influence of porosity. *Geochemica et Cosmochimica Acta*, 57, 571-578.

Incropera, F.P., D.P. Dewitt, T.L. Bergman, & A.S. Lavine (2007), Fundamentals of Heat and Mass Transfer, John Wiley, Hoboken, NJ.

1435 Kessler, A.J., Glud, R.N., Cardenas, M.B., & Cook, P.L.M. (2013), Transport zonation
1436 limits coupled nitrification-denitrification in permeable sediments. *Environmental*
1437 *Science and Technology*, 47, 13404-13411.

1438 Knapp, J.L.A., Gonzalez, Pinzon, R., Drummond, J.D., Larsen, L.G., Cirpka, O.A., &
1439 Harvey, J.W. (2017), Tracer-based characterization of hyporheic exchange and benthic
1440 biolayers in streams. *Water Resources Research*, 53, 1575-1594.
1441 https//doi:10.1002/2016WR019393

1442 Krause, S., Lewandowski, J., Grimm, N. B., Hannah, D. M., Pinay, G., McDonald, K., et
1443 al. (2017), Ecohydrological interfaces as hot spots of ecosystem processes. *Water*
1444 *Resources Research*, 53(8), 6359–6376. https//doi:10.1002/2016WR019516

1445 Kumar, S.S., Kozarek, J., Hornbach, D., Hondzo, & M., Hong, J. (2019), Experimental
1446 investigation of turbulent flow over live mussels. *Environmental Fluid Mechanics*.
1447 https//doi:10.1007/s10652-019-09664-2

1448 Laube, G., Schmidt, C., & Fleckenstein, J.H. (2018), The systematic effect of streambed
1449 conductivity heterogeneity on hyporheic flux and residence time. *Advances Water*
1450 *Research,* 122, 60-69.

1451 Leibundgut, C., Maloszewski, P., & Kulls, C. (2009) "Tracers in Hydrology" (1st Ed).
1452 Chichester, UK; Hoboken, NJ: Wiley.

1453 Liem, R., Spork, & V., Koengeter, J. (1997), Investigations on erosional processes of
1454 cohesive sediment using an in-situ measuring device. *International J. Sediment Research*,
1455 13, 139-147.

1456 Manuel, J. (2014), Crisis and Emergency Risk Communication: Lessons from the Elk
1457 River Spill. *Environmental Health Perspectives*, 122(8), A215-A219.

1458 Marion A., & M. Zaramella (2015) Diffusive behavior of bedform-induced hyporheic
1459 exchange in rivers. *J. Environ. Eng*., 131(9), 1260-1266, doi: 10.1061/(ASCE)0733-
1460 9372(2005)131:9(1260).

1461 Meter, K.J.V., Basu, N.B., & Van Cappellen, P.V. (2017) Two centuries of nitrogen
1462 dynamics: Legacy sources and sinks in the Mississippi and Susquehanna River Basins.
1463 *Global Biogeochemical Cycles*, 31, 2-3. https//doi:10.1002/2016GB005498

1464 Meter, K.J.V., Cappellen, P.V., & Basu, N.B. (2018), Legacy nitrogen may prevent
1465 achievement of water quality goals in the Gulf of Mexico. Science,
1466 https//doi:10.1126/science.aar4462.

1467 Myers, G.E. (1971), Analytical methods in conduction heat transfer, McGraw-Hill, New
1468 York.

1469 Nagaoka, H., & Ohgaki, S. (1990), Mass transfer mechanism in a porous riverbed. *Water*
1470 *Research* 24(4), 417-425.

1471 Newcomer, M.E., Hubbard, S.S., Fleckenstein, J.H., Maier, U., Schmidt, C., Thullner,
1472 M., et al. (2016), Simulating bioclogging effects on dynamic riverbed permeability and
1473 infiltration. Water Resources Research, 52(4), 2883-2900.
1474 https://doi.org/10.1002/2015WR018351

1475 O'Connor, B.L. & Harvey, J.W. (2008), Scaling hyporheic exchange and its influence on
1476 biogeochemical reactions in aquatic ecosystems. *Water Resources Research*, 44,
1477 W12423. https//doi:10.1029/2008WR007160

1478 O'Connor, B.L., Harvey, J.W., & McPhillips, L.E. (2012), Thresholds of flow-induced
1479 bed disturbances and their effects on stream metabolism in an agricultural river. *Water*
1480 *Resources Research*, 48, W08504. https//doi:10.1029/2011WR011488

1481 O'Connor, B.L., & Hondzo, M. (2008), Dissolved oxygen transfer to sediments by sweep
1482 and eject motions in aquatic environments. *Limnology and Oceanography*, 53(2), 566-
1483 578.

1484 Oldham, C.E., Farrow, D.E., & Peiffer, S. (2013), A generalized Damkholer number for
1485 classifying material processing in hydrological systems. *Hydrology and Earth Systems*
1486 *Sciences*, 17(3), 1133-1148. https://doi.org/10.5194/hess-17-1133-2013

1487 Packman, A.I., M. Salehin, M., & Zaramella, M. (2004), Hyporheic exchange with gravel
1488 beds: Basic hydrodynamic interactions and bedform-induced advective flows. *ASCE J.*
1489 *Hydraulic Engineeering*., 130(7), 647-656.

1490 Perez Guerrero, J.S., Pontedeiro, E.M. van Genuchten, M.Th., Skaggs, T.H. (2013),
1491 Analytical solutions of the one-dimensional advection-dispersion solute transport
1492 equation subject to time-dependent boundary conditions. *Chemical Engineering Journal*,
1493 221, 487-491.

1494 Pokrajac, D., & C. Manes (2009), Velocity measurements of a free-surface turbulent flow
1495 penetrating a porous medium composed of uniform-size spheres, *Transp. Porous Med.*
1496 78(3), 367–383, doi:10.1007/s11242-009-9339-8.

1497 Reidenbach, M.A., Limm, M., Hondzo, M., & Stacey, M.T. (2010), Effects of bed
1498 roughness on boundary layer mixing and mass flux across the sediment-water interface.
1499 *Water Resources Research,* 46, W07530. https//doi:10.1029/2009WR008248

1500 Richardson, C.P., & Parr, A.D. (1988), Modified Fickian model for solute uptake by
1501 runoff. *ASCE J. Environmental Engineering*, 114, 792-809.

1502 Roche, K.R., Blois, G., Best, J.L., Christensen, K.T., Aubeneau, A.F., & Packman, A.I.
1503 (2018), Turbulence links momentum and solute exchange in coarse-grained streambeds.
1504 *Water Resources Research*, 54, 3225-3242. https//doi:10.1029/2017WR021992

1505 Roche, K.R., Li, A., Bolster, D., Wagner, G.J., & Packman, A.I. (2019), Effects of
1506 turbulent hyporheic mixing on reach-scale transport. *Water Resources Research*, 55,
1507 3780-3795.

1508 Salehin, M., Packman, A.I., & Paradis, M. (2004), Hyporheic exchange with
1509 heterogeneous streambeds: Laboratory experiments and modeling. *Water Resources*
1510 *Research,* 40, W11504.

1511 Schmadel, N.M., Harvey, J.W., Schwarz, G.E., Alexander, R.B., Gomez-Velez, J.D.,
1512 Scott, D., & Ator, S.W. (2019), Small ponds in headwater catchments are a dominant
1513 influence on regional nutrient and sediment budgets, Geophysical Research Letters,
1514 46(16), 9669-9677. https://doi.org/10.1029/2019GL083937

1515 Sport, V., Jahnke, J., Prochnow, J., & Koengeter, J. (1997), Stabilising effect of benthic
1516 algae on cohesive sediments, *International J. Sediment Research*, 12, 399-406.

1517 Stewardson, M.J., Datry, T., Lamouroux, N., Pella, H., Thommeret, N., Valette, L.,
1518 Grant, S.B. (2016), Variation in reach-scalke hydraulic conductivity of streambeds.
1519 *Geomorphology*, 259, 70-80.

1520 Thibodeaux, L.J., & Boyle, J.D. (1987), Bedform-generated convective transport in
1521 bottom sediment. *Nature*, 325, 341-343.

1522 Tomasek, A.A., Barman, T.D., Wang, P., Kozarek, J.L., Staley, C., Sadowsky, M.J., &
1523 Hondzo, M. (2018). The effects of turbulence and carbon amendments on nitrate uptake
1524 and microbial gene abundances in stream sediment. *J. Geophysical Research:*
1525 *Biogeoscience*, 123, 1289-1301. https//doi:10.1002/2017JG004261

1526 Trauth, N., Schmidt, C. Vieweg, M., Maier, U., & Fleckenstein, J. H. (2014), Hyporheic
1527 transport and biogeochemical reactions in pool-riffle systems under varying ambient
1528 groundwater flow conditions. *Journal Geophysical Research: Biogeosciences*, 119, 910-
1529 928. https//doi:10.1002/2013JG002586

1530 Van Genuchten, M.T., Leij, F.J., Skaggs, T.H., Toride, N., Bradford, S.A., & Pontedeiro,
1531 E.M. (2013), Exact analytical solutions for contaminant transport in rivers. 2 Transient
1532 storage and decay chain solutions. *J. Hydrological Hydromechanics*, 61, 250-259.

1533 Veslind, P.A. "Introduction to Environmental Engineering", Boston, MA, PWS
1534 Publishing Co., 1st Ed.

1535 Voermans, J. J., Ghisalberti, M., & Ivey, G. N. (2017), The variation of flow and
1536 turbulence across the sediment-water interface. *Journal of Fluid Mechanics*, 824, 413-
1537 437. https//doi:10.1017/jfm.2017.345

1538 Voermans, J. J., Ghisalberti, M., & Ivey, G. N. (2018), A model for mass transport across
1539 the sediment-water interface. *Water Resources Research*, 54, 2799-2812.
1540 https//doi:10.1002/2017WR022418

1541 Walsh, C.J., Roy, A.H., Feminella, J.W., Cottingham, P.D., Groffman, P.M., & Morgan,
1542 R.P. (2005), The urban stream syndrome: current knowledge and search for a cure. *J. N.*
1543 *Am. Benthol. Soc.*, 24(3), 703-723.

1544 Weidhaas, J.L., Dietrich, A.M., DeUYonker, N.J., et al. (2016), Enabling science support
1545 for better decision-making when responding to chemical spills. J. Environmental Quality,
1546 45(5) 1490-1500. https//doi:10.2134/jeq2016.03.0090

1547 Wörman, A., Packman, A.I., Marklund, L., Harvey, J.W., & Stone, S.H. (2007), Fractal
1548 topography and subsurface water flows from fluival bedforms to the continental shield.
1549 *Geophysical Research Letters,* 34(7), L07402. https//doi:10.1029/2007GL029426

1550 Wu, L. Singh, T., Gomez-Velez, J., Nutzmann, G., Worman, A., Krause, S.,
1551 Lewandowski, J. (2018) Impact of dynamically changing discharge on hyporheic
1552 exchange processes under gaining and losing groundwater conditions. Water Resources
1553 Research, 54(12), 10076-10093. https://doi.org/10.1029/2018WR023185

1554 Yates, S.R. (1992), An analytical solution for one-dimensional transport in porous media
1555 with an exponential dispersion function. *Water Resources Research*, 28(8), 2149-2154.

1556 Zarnetske, J. P. Haggerty, R., Wondzell, S. M., & Baker, M. A. (2011), Dynamics of
1557 nitrate production and removal as a function of residence time in the hyporheic zone.
1558 Journal of *Geophysical Research: Biogeosciences*, 116(G1), G01025.
1559 https//doi:10.1029/2010JG001356

1560 Zheng, L., Cardenas M.B., Wang, L., & Mohrig, D. (2019) Ripple effects: bedform
1561 morphodynamics cascading into hyporheic zone biogeochemistry. *Water Resources*
1562 *Research,* Advanced online publication. https//doi:10.1029/29018WR023517

1563 Zhong, Q., Chen, Q., Wang, H., Li, D., Wang, X. (2016), Statistical analysis of turbulent
1564 super-streamwise vortices based on observations of streaky structures near the free
1565 surface in the smooth open channel flow. *Water Resources Research*, 52, 3563–3578.
1566 https//doi:10.1002/2015WR017728